INSIGHT IN TO THE SURFACE AND SUBSURFACE EXPRESSIONS OF BURANGA GEOTHERMAL FIELD, UGANDA

DSM CHANDIMA FERNANDO

February, 2012

SUPERVISORS:

Dr. M. (Mark) van der Meijde

Mr. C.A. (Chris) Hecker (MSc)

INSIGHT IN TO THE SURFACE AND SUBSURFACE EXPRESSIONS OF BURANGA GEOTHERMAL FIELD, UGANDA

DSM CHANDIMA FERNANDO
Enschede, The Netherlands, February, 2012

Thesis submitted to the Faculty of Geo-Information Science and Earth Observation of the University of Twente in partial fulfilment of the requirements for the degree of Master of Science in Geo-information Science and Earth Observation.
Specialization: [Name course (e.g. Applied Earth Sciences)]

SUPERVISORS:
Dr. M. (Mark) van der Meijde
Mr. C.A. (Chris) Hecker (MSc)

THESIS ASSESSMENT BOARD:
Prof. Dr.F.D. van der Meer (Chair)
Dr. Mike Buxton (External Examiner) Department of Geotechnology – Civil-Engineering & Geosceinces, University of Delft

DISCLAIMER

This document describes work undertaken as part of a programme of study at the Faculty of Geo-Information Science and Earth Observation of the University of Twente. All views and opinions expressed therein remain the sole responsibility of the author, and do not necessarily represent those of the Faculty.

ABSTRACT

Previous seismic studies over the Buranga area, Uganda have identified an evidence for the existence of a hot degassing magma body in the subsurface which is considered as the heat source for the Buranga hot springs. Surface geothermal expressions identification over the Buranga geothermal field in Uganda and its link to the subsurface geothermal source are the main objective of this study.

Various types of remotely sensed data were used to pinpoint the surface geothermal expressions. To indicate hot spring alteration minerals, band ratio of SWIR ASTER bands, after masking vegetation, (B5+B7)/B6, (B6+B9)/(B7+B8) and B5/B4 respectively was used to indicate the occurrence of Al-OH containing minerals, Mg-OH containing minerals and gypsum. The sub pixel size hot spot identification method was applied to the MODIS aqua night thermal Infrared images to identify the surface temperature anomalies associated with geothermal activities. The resulted ratio images of the radiant temperature images were threshold using hotspot identification algorithm. The 3 directional hill shaded ASTER Global DEM version 2 and the directionally filtered multispectral ASTER band 2 were used to identify the surface geological structures.

The distribution of the minerals containing Al-OH as a main absorption feature was found mainly related to clay minerals in flood plains (also within rivers) and less around hot springs due to alteration. The band ratio that was used for Mg-OH containing minerals didn't enhance the hot springs area and only identified the areas where carbonate is dominant as calcareous sandstone due to CO_3^{2-} bond which overlaps the Mg-OH absorption feature. The areas outlined after applying the band ratio for gypsum were found mainly in recent sediments, lakes and close to oil seepages.The temperature variation of the area is mostly governed by the vegetation and moisture contents. The resulted pixels with hotspot from thresholding values of the ratio images of radiant temperature don't show any relation to the geothermal hot springs. Hotspot pixels, after applying hotspot detection algorithms, were found related to places rich in water content such as flood plains along rivers and crater lakes. The surface structural interpretation indicated three prominent lineament patterns, NNE normal faults demarcating the rift valley and Ruwenzori mountain block; and two linear features trending NW and NE to ENE. The Buranga hot spring is located on one of the NE trending lineament on the rift valley.

Integration of the seismic P wave velocity anomalies with the interpreted structural map showed a relationship between the surface structural faults and the subsurface intrusion body which is thought to be the feeder of the hot springs throughout the upwelling hot fluids along these faults.

ACKNOWLEDGEMENT

First and foremost my sincere thank goes to my supervisors Dr. Mark van der Meijde and Mr. C.A. Chris Hecker for their constant guidance and encouragement thought out my research period.

I would like offer my gratitude to Ms. Geraldine Paula Babirye from Geological Survey of Uganda for her kind support for me to have secondary data for my study.

I also would like to thank Prof. Freek van der Meer, The Chairman of the Earth System Analysis Department, all the AES staff teachers, especially the teachers in mineral exploration section for the knowledge and instructions they gave in my studies at ITC.

I am thankful to the former AES Course Director Drs. Tom Loran and the present AES Course Director Dr. Harald Van der Werff for their enormous support in challenging and problematic conditions in my study period.

I am really grateful to all my friends in AES group and all the other friends at ITC who make me feel comfortable throughout the stay at ITC.

My family and all my friends back home, my heartiest gratitude to you all for the emotional support and affection you gave me in each and every moment of my life.

TABLE OF CONTENTS

LIST OF FIGURES

LIST OF TABLES

ABBREVIATIONS

1D	One-dimensional
2D	Two-dimensional
ASTER	Advanced Spaceborne Thermal Emission and Reflection Radiometer
DEM	Digital Elevation Model
ENVI	Environment for Visualizing Images
MODIS	Moderate Resolution Imaging Spectroradiometer
NDVI	Normalized Difference Vegetation Index
SWIR	Short-Wave Infrared
TIR	Thermal Infrared
VNIR	Visible and Near Infrared

1. INTRODUCTION

1.1. Research background

The geothermal potential of Africa is mostly related with the east African rift valley area. Uganda has the opportunity to have geothermal potential area which is indicated by a number of hot springs. Previous studies shows that Ruwenzori mountain area is most consider being having geothermal manifestation within Uganda. So far there are several hot springs, fumaroles has been found which are related with the Buranga area (Bahati et al., 2005). The subsurface heat source responsible for the formation of the Buranga hot spring has been suggested by the previous seismic studies. Maasha (1975) has identified a higher micro earthquakes activity within the Ruwenzori area) more than other regions in Uganda. Among that Buranga area has showed the highest seismicity level. Based on that, Ochamann et al. (2010) has carried out a tomographic inversion of seismic travel time data to find out the heat source for the Buranga hot springs assuming that the geothermal source is a hot actively degassing magma body in the subsurface. The study by Ochamann et al. (2010) has identified a significant reduce in the local velocity at the base of the Ruwenzori mountain subsurface and the reduction is strong within 1-5 kms below the surface. Further, Ochamann et al. (2010) mentioned that the isotope composition of CO_2 releasing from the Buranga hot spring is compatible with that of the mantle. Therefore the conclusion is that the low seismic velocity anomaly is due to an actively degassing magma intrusion and it is related to source of the hot springs. According to the conceptual model of Ochamann et al. (2010) water recharging from the Ruwenzori mountainous region heats up due to this hot magmatic body and that water upwells along the faults towards the rift system.

1.2. Problem statemet

However, the model has no resolution in the first one kilometre from the surface. What still needs to be resolved is on how the structural surface features can link the surface expressions of the area to the subsurface heat source. If this Buranga geothermal area can be detected using remote sensing methods and the association can be established between surface features and subsurface heat source, the identification criteria can be applied in to the other prospective areas along the rift zone where there is no much idea about the subsurface. The previously done seismic survey in Buranga will support to link the surface geothermal features to the subsurface.

1.3. Research objectives

The main objective of this research is to understand the spatial relationship between geothermal subsurface sources and their surface expressions in Buranga geothermal field. .

Sub objectives:

1. To identify the surface mineral alterations systems based on VIS-SWIR-TIR remote sensing techniques
2. To identify thermal anomalies due to a geothermal source using night time thermal imagery
3. To identify surface structural features using elevation data and VIS/SWIR satellite images
4. To define the link of the geothermal source with geological structures and geothermal surface expressions

1.4. Research questions

1. 2. What is the spatial distribution of the hydrothermal alteration systems?

2. What is the spatial distribution of the thermal anomalies?
3. What is the spatial distribution of geological structures?
4. What is the spatial association of the geothermal surface expressions and geological structures with the heat source?

1.5. Hypothesis

1. Detectable mineralogy within VIS-SWIR-TIR regions allows determining alteration systems in the study area.
2. Thermal remote sensing technique can be used to identify the surface thermal anomalies in this area
3. The elevation data (DEM) and multi spectral remote sensing data is productive in extracting surface geological structures.
4. There is a spatial relation between surface indicators and subsurface presence of geothermal source

1.6. Thesis Structure

Chapter 1: Introduction
This chapter explains the research questions, objectives of the studies and the hypothesis.
Chapter 2: Literature review
This chapter contains location and geology of the study area, useful information about the geothermal indicators and the much more details on the tomographic inversion model of the seismic data of Buranga area.
Chapter 3: Methodology
All the data set and methods which were used to fulfil objectives has been explained in this chapter.
Chapter 4: Result and discussion
This chapter focused on the results of the structural interpretation, thermal anomaly mapping and mineral alteration identification and their relation to the subsurface heat source. .
Chapter 5: Conclusions and Recommendations
This concluding chapter contains the conclusions derived on the results and recommendations for further studies.

2. LITERETURE REVIEW

This chapter will give an overview of the location of the study area, general geological and structural setting, geothermal activities within Albertine rift valley, details on the seismic tomographic model leading to the subsurface heat source for the Buranga geothermal field and possible geothermal expressions on a geothermally manifested area.

2.1. Study area

2.1.1. Location

The study area is located on the western part of Uganda. It is about i225km^2 in surface coverage and lies within the coordinates of 0.5^{0}N to 1.0^0 N of latitude and 29.9^0 E to 30.3^0 E of longitudes (UTM WGS 1984 Zone 35N) (Figure 2.1). The study area was selected as it covers the area which is shown by the tomographic model in the section 2.4.

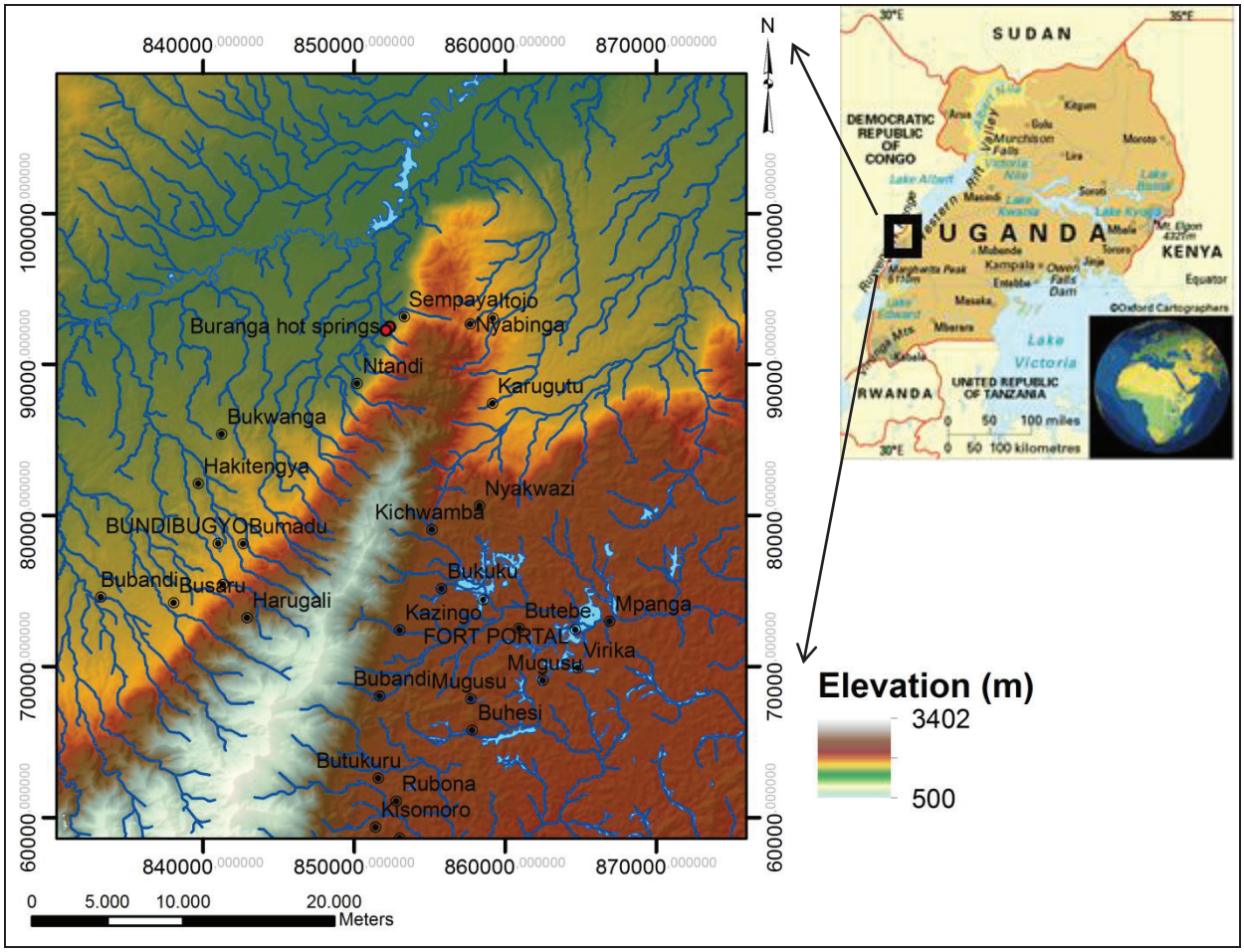

Figure 2.1: Extent, drainage system and topography of the study area (left); Location of the study area (www.thecommonwealth.org) (right)

The elevation of the area is ranging from 800m up to 3402m (Figure 2.1). Geographically, this area consists of highly elevated Mountain called Ruwenzori and flat land surrounding the mountain.

2.1.2. Surface land cover and climate

The Ruwenzori mountain is almost covered with dense vegetation. The flat terrain west to the Ruwenzori Mountain is also partly covered with dense vegetation and called as Semuliki National Park. Other areas are partially covered with agricultural lands, sparse vegetation, swamps and lakes. The north to the mountain is mainly covered with grass(Ochmann, et al., 2010). This study area has tropical weather conditions and there is an annual change in climate from dry to wet seasons. Dry season falls within December to February and June to August (www.climatetemp.info). The Ruwenzori mountain region is a good water catchment and the considerable amount of rainfall can be expected even in the dry seasons (Eggermont et al., 2007).

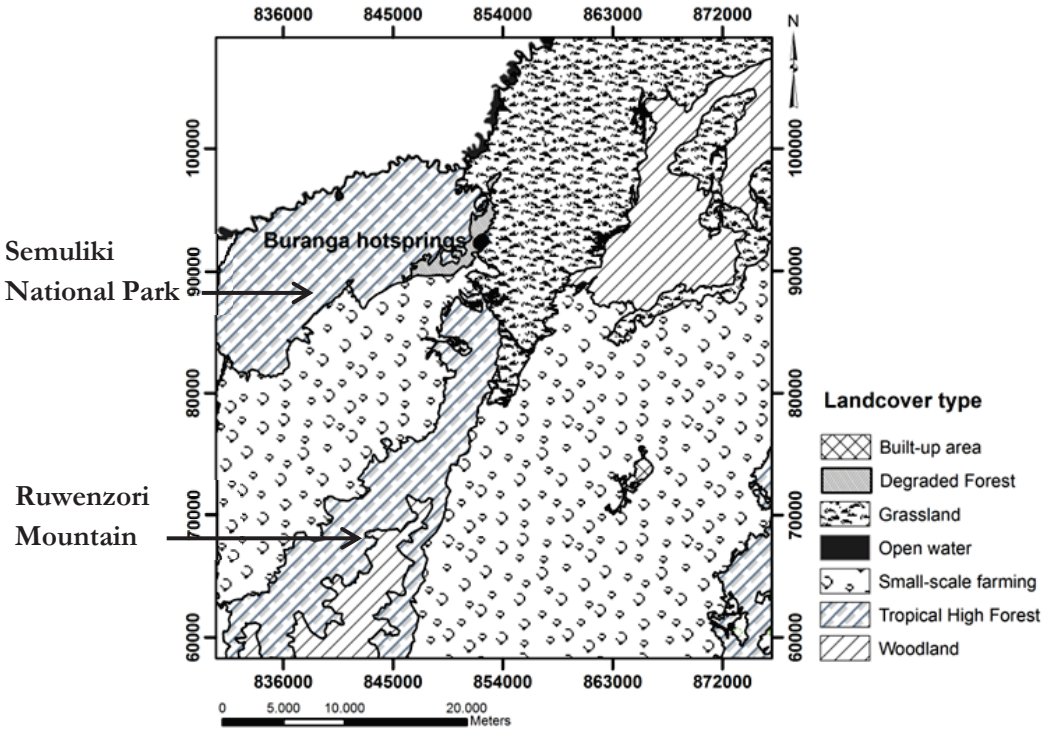

Figure 2.2: Land cover map prepared using the digital data from Geological Survey of Uganda

2.1.3. Geology and tectonic setting of Albertine rift valley area

East African rift system has originated in the early tertiary from the Afar hot spot, at the Red Sea and has extended with time to the south of Malawi. This normal fault rift system is narrowing down from north to south showing decreasing crustal separation and magmatic intensity (Saemundsson, 2010). Along the rift valley, the Achaean crystalline basement is mainly covered with tertiary volcanic rocks. However some areas are covered with Mesozoic sediments (Woldegabriel et al., 1990). East African rift valley zone is composed of extensional normal faults, NW striking transform faults and strike slip faults (Chorowicz, 2005).

The western branch of the East African rift valley system which is passing through Uganda is associated with few volcanoes and deep lakes. Albertine rift is the upper part of this western branch. Albertine rift valley zone is mostly composed of the Miocene to recent rift sediments. The highly elevated Ruwenzori mountain and eastern side of the mountain is composed of Achaean basement gneissic rocks (Koehn et al., 2010)There is an indication of the volcanic activities like volcanic rocks and craters to the east and

south of the Ruwenzori Mountain but not in the western side (Figure 2.3). The rift sediment considered to be synrift and the thickness of the sediment cover is ranging from 350m to 600m (Roller et al., 2010). The sediments cover is composed of swampy deposits, alluvium, lacustrine deposits, sands, sandstones and siltstones (Maasha, 1975). The Figure 2.4, the cross section cutting Ruwenzori mountain and rift valley cleary indicates the present geological setting of the area with reference to the Ruwenzori mountain block and the rift.

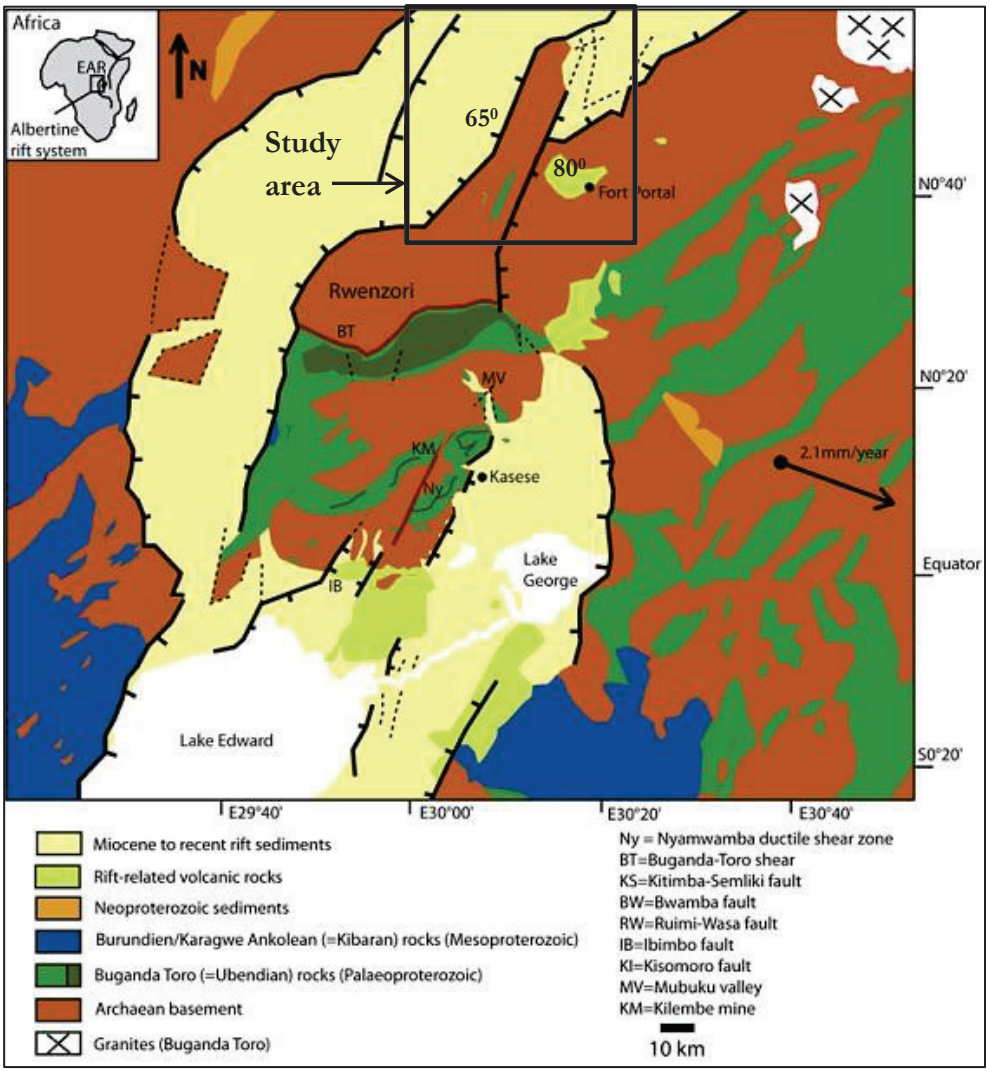

Figure 2.3: Simplified geological map of the Ruwenzori area (Koehn, et al., 2010)

Ruwenzori Mountain is trending NNE direction. The field measurements carried out by Koehn et al. (2008) has found that Albertine rift valley has formed collectively with the dextral strike-slip and normal faults. Hence the boundary between rift and mountains shows a zigzag shape. The normal fault which is running along the western flank of Ruwenzori mountain is called as Buwampa fault and it is dipping towards west with an angle of 65^0.

On the Ruwenzori mountain top, 3 sets of faults have been identified. Steeply dipping two sets of faults trending NW–SE (mixed dextral strike slip and normal) and N–S (normal to strike slip faults) and one set of moderately dipping normal fault trending E–W to ENE–WSW. In the northern part of the mountain consist of two fault system which is parallel to the mountain strike and cross cutting set of faults trending

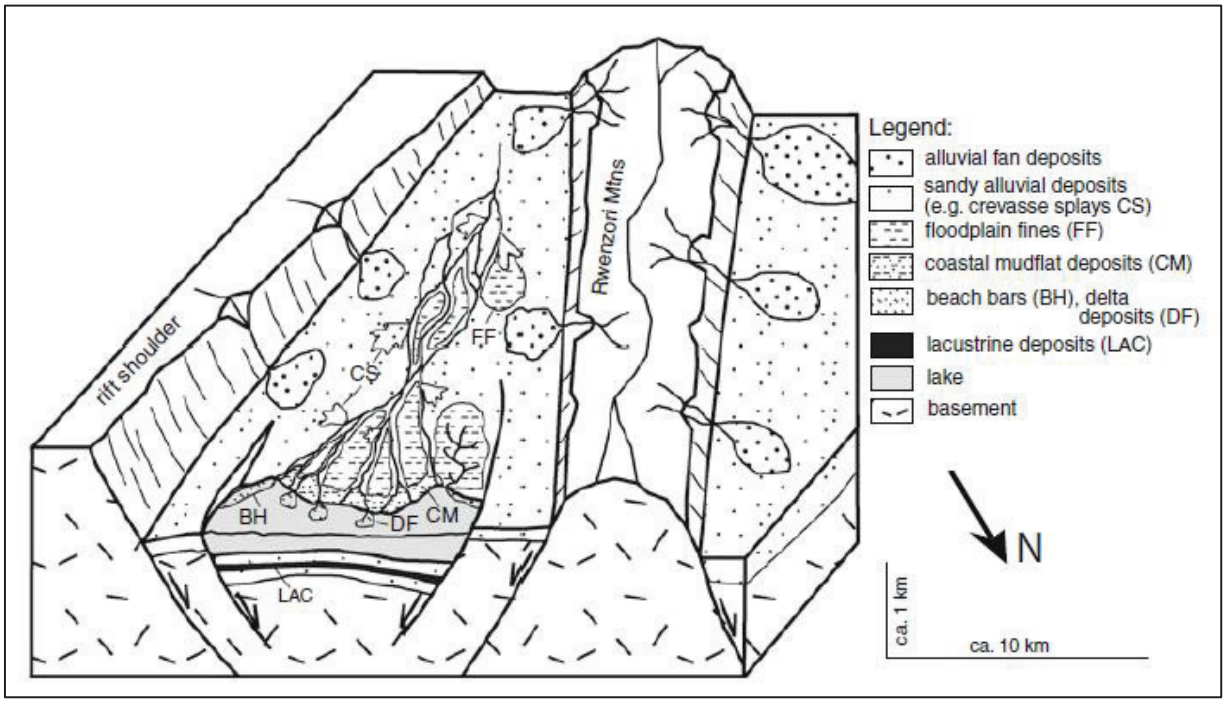

Figure 2.4: 3D diagram of the depositional scenario over the Albertine rift valley (Roller, et al., 2010)

NE–SW. Koehn et al, (2008) have also identified two major systems at the north eastern side of the Ruwenzori mountain. Those are the SSW–NNE (parallel to Ruwenzori mountain range) and ESE–WNW. Two minor fault systems are running N–S and E–W direction.

There is an indication of a fault which is running through the Buranga hot spring according to the field studies by Bahati (1998). This is named as hot spring fault. It is trending $N50^0$ E and cross cut the Buwampa fault (Figure 2.5).

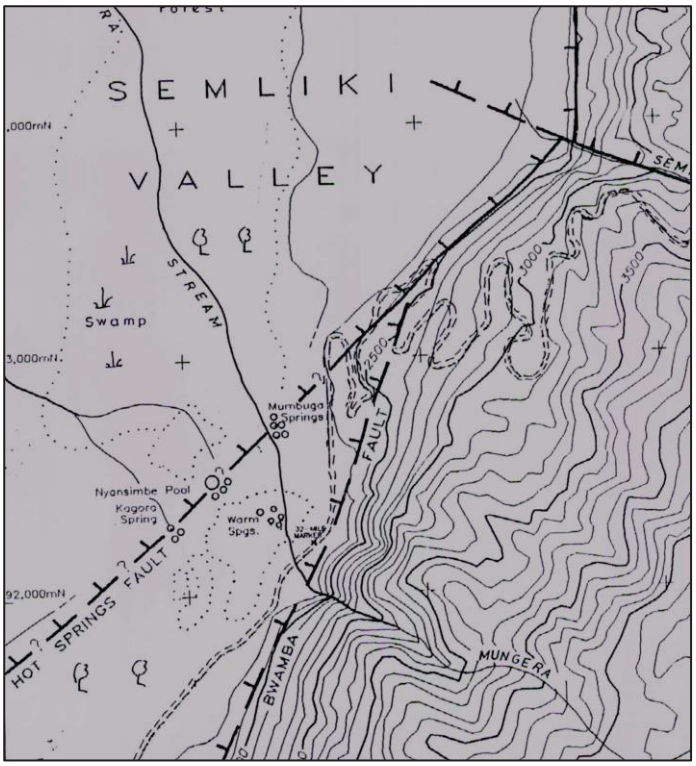

Figure 2.5: The hot spring fault cross cut the Buranga hot spring (Bahati, 1998)

2.2. Chatracteristics of the geothermal fields around Ruwenzori mountain

As shown in Bahati (2005), there are three major areas, Katwe-Kikorongo (Katwe), Buranga and Kibiro (Figure 2.6) which are considered to have potential for geothermal resources in southern Uganda and all three areas lie along the rift valley zone. .

Buranga, which is the study area of this research, is at the base of north western side of the Ruwenzori Mountain between Lake Edward and Lake Albert (figure 2.6). Basement rocks of Buranga are mostly covered with tertiary sediments (calcareous sandstone). Several hot springs and high gas flows indicate geothermal activities in the Buranga area while this area does not show any volcanism or intrusive dikes (Bahati, et al., 2005);(Ochmann, et al., 2010). Further, another indication for the geothermal activity of the area is the zone of travertine deposits stretching for 10km north to Buranga hot springs (Natukunda, 2010). The formation of travertine (formed by the reaction of calcium in the hot water with the atmospheric CO2) is a good indicator for geothermal groundwater activities (Coolbaugh et al., 2009).

The Kibiro area (Figure 2.6), at the eastern escarpment of the rift, consists of crystalline basement of granitic and granitic gneiss and is overlain by a thick sequence of sediments at the rift zone. The presence of myolinite and brecciated rocks manifested the highly faulted environment (Natukunda, 2010). (Natukunda, 2010) has mentioned that hot and warm springs, steaming ground, altered rocks and calcite deposits found in cracks and fissures of granite are indications of geothermal potential of the area. Further, these characteristic features are associated with the fault system of the area. For instance, the main hot springs area is found at the base of the NS trending main fault escarpment.

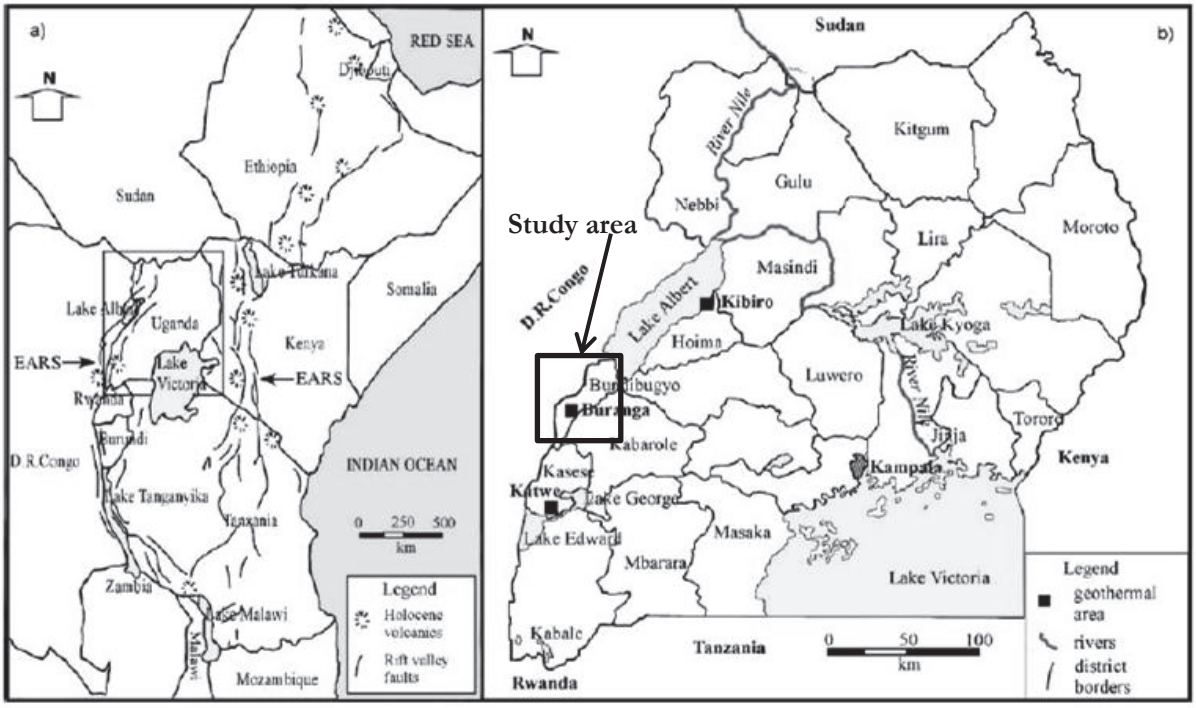

Figure 2.6: The East African Rift System (EARS) and (b) location of the three main geothermal areas in Uganda (Katwe, Buranga and Kibiro). D.R.C., Democratic Republic of Congo (Bahati et al., 2005)

The Katwe geothermal prospective area is situated north of the Lake Edward (figure 1) and in the western escarpment of the rift zone. Unlike in Kibiro and Buranga, Katwe area is on a volcanic field which consists of hundreds of eruptive centres of phreatic volcanoes(Natukunda, 2010). Phreatic volcanoes are formed due to the interaction of hot magma with ground water. Basement rocks are overlain by pyroclastic volcanic rocks and the rift valley area is covered with lake sediments. As shown in Natukunda (2010), hot spring, warm springs and travertine deposits are indicators of geothermal activity in the area.

2.3. Seisemic travel time tomographic study on the Ruwenzori mountain area

This description is based on inversion the seismic velocity difference of seismic travel time to a 3D tomographic model by Ochmann et al. (2010). This study has used records of local earthquakes around Ruwenzori mountain block retrieved from January to April 2006 using nine seismometer. and from April to August 2006 using 15 seismometers. Due to the localization of earthquake are having bias errors, the 3D velocity model has been applied for the seismic data.

The P wave velocity anomaly model is considered to be better than S wave velocity model as the S wave velocity detection has blunders more than in P wave velocity detection. The tomographic model of the P wave velocity anomaly shows the increase in velocity difference when going deep. The speed of seismic waves becomes lower at the liquid state of materials. Hence the low velocity anomalies indicate high temperature low dense materials at the subsurface that is a hot degassing magma body. It is considered to be a melt as it didn't show any magnetism and temperature is thought to be in the Curie point. When the rocks melt below the Curie temperature and lost its magnetic properties. Ochmann et al. (2010) suggest that this anomaly represent the heat source for the Buranga hot springs. The dV/V% values represent the

percentage of the delay of P wave anomalies with reference to reference value. The values less than zero indicate the hot body.

The strong shallow level (1-5km) anomaly is visible close to the Buwampa normal fault. They have found that the -9% seismic anomaly at 10km depth directs towards the Buranga hot spring on the surface (Figure 2.7).

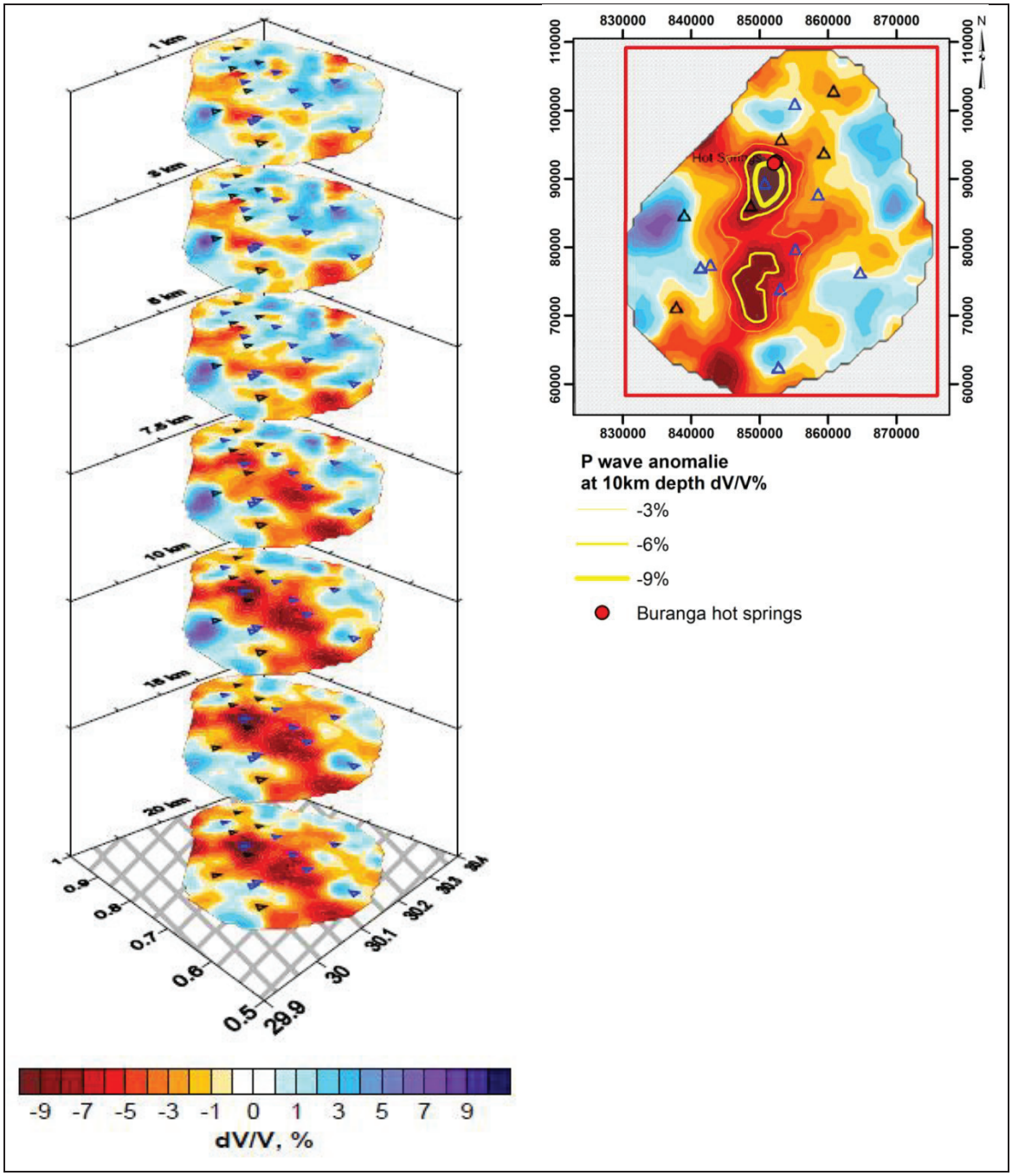

Figure 2.7: The horizontal sections of the P wave anomalies at different depth levels (left); Buranga hot spring location plotted on 1okm depth P wave anomalies(right) (Ochmann, et al., 2010)

Moreover Ochmann, et al. (2010) has suggested a conceptual model; for the Buranga geothermal field activity based on the suggested heat source (Figure 2.8). According to the model, meteoric water penetrates through fractures of the Ruwenzori mountain block and heat up with the heat source. Finally the hot fluid emits through the rift valley sediments. As per to this model the Buranga geothermal system Buranga geothermal field is structurally controlled.

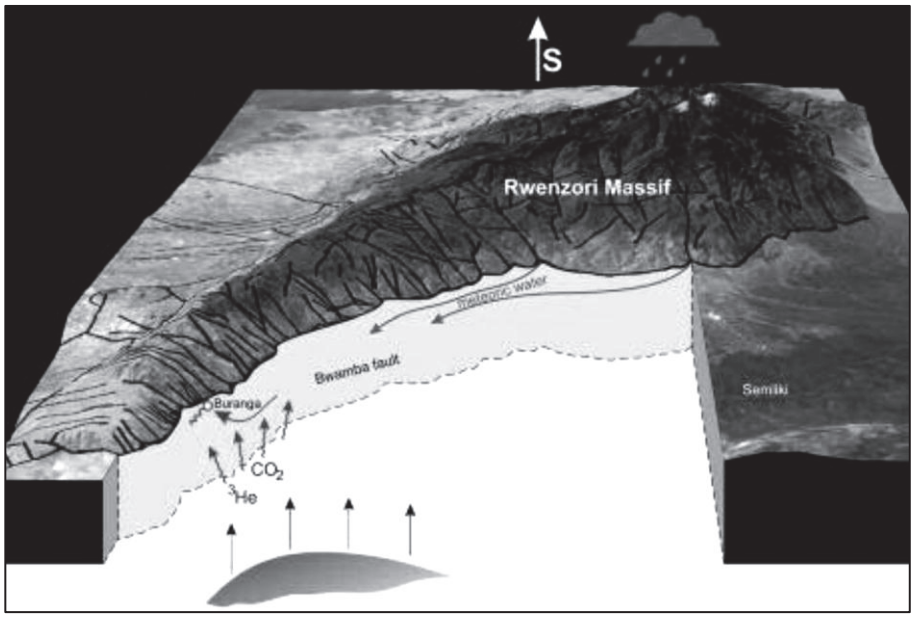

Figure 2.8: Three dimensional view of the Ruwenzori mountain overlain by a lineament pattern and integrated conceptual model.(Ochmann, et al., 2010)

2.4. Surface geothermal indicators

Heat source, fracture and fluids are the major components of a geothermal system (Hanano, 2004). Geothermal water heated up with geothermal heat source and rose through the fractures. This high temperature fluid comes out to the surface makes visible changes on the surrounding. The hot liquid comes out as features like hot springs, fumaroles, boiling pools, hot and steaming grounds and geysers. And the ground shows the elevated temperature values and warm surfaces (Coolbaugh et al., 2007)

The other indication is the altered minerals. The geology of the ground become instable with high temperature and altered to new minerals reacting with the hot fluids. The type of altered minerals depends on the chemistry of the host rock, the chemistry of the geothermal fluid and the temperature of the fluid(Kühn, 2004).

The thermally stressed vegetation is another kind of indication in the geothermally active areas (Eneva et al., 2006).

3. MATERIALS AND METHODS

3.1. Dataset

Several types of satellite and legacy data were utilized in the research work. The coordinate system WGS 1984 Zone 32 was applied for all the data.

3.1.1. Elevation data

As follows two types of DEM data with different spatial resolution was used for the study.

1. SRTM DEM

SRTM DEM has the spatial resolution of 90m. This data was downloaded free of charge from the website Global Land Cover Facility (GLCF) website by NASA (http://glcf.umiacs.umd.edu/).

2. ASTER Global DEM version2

ASTER Global DEM has the 30m spatial resolution. For the study ASTER 30m resolution new version was downloaded free of charge from the ASTER Global DEM website (http://www.gdem.aster.ersdac.or.jp/). The new version of the ASTER DEM has increased horizontal and vertical accuracy, better horizontal resolution, reduced presence of artifacts, and more realistic values over water bodies more than in the old version of ASTER DEM (USGS, 2011).

3.1.2. Advanced Thermal Emission and Reflection Radiometer (ASTER) images

The ASTER multispectral data consists of 15 bands (Table 3.1). First four bands belong to VNIR region of the electromagnetic spectrum. Next six is on the SWIR region and TIR region is covered by Band 10 to band 14 (NASA, 2004).

Table 3.1: Multispectral ASTER Band details

Band Number	Wavelength (**μm**)	Wavelength region	Spatial Resolution (m)
B1	0.52 - 0.60	VNIR	30
B2	0.63 - 0.69	VNIR	30
B3b	0.76 - 0.86	VNIR	30
B3n	0.76 - 0.86	VNIR	30
B4	1.60 - 1.70	SWIR	60
B5	2.145 - 2.185	SWIR	60
B6	2.185 - 2.225	SWIR	60
B7	2.235 - 2.285	SWIR	60
B8	2.295 - 2.365	SWIR	60
B9	2.36 - 2.43	TIR	90
B10	8.125 - 8.475	TIR	90
B11	8.475 - 8.825	TIR	90
B12	8.925 - 9.275	TIR	90
B13	10.25 - 10.95	TIR	90
B14	10.95 - 11.65	TIR	90

ASTER images were downloaded through the ITC geo-data ware house. The aster scene were downloaded with cloud content is less than 2%. Two aster scenes which were used for the study has been

acquired on 02nd of February in 2005 and other has been acquired on 05th of July 2004. Those dates fall within the dry seasons of the area with less rain fall.

1. AST_L1B Registered Radiance at the Sensor data

The original AST_L1B Registered Radiance at the Sensor data had been radio-metrically calibrated to radiance at sensor values. Further these images had been co-registered for the geometric errors arise due to terrain elevation differences (www.lpdaac.usgs.gov).

2. AST_ 07XT Surface Reflectance data

In original AST_ 07XT Surface Reflectance images, All VNIR and SWIR bands had been corrected for the atmospheric effect and converted to the surface reflectance values. The SWIR bands had been cross talk corrected to reduce the energy leaking from band 4 to band 5 and 9. Therefore it is not necessary to do the atmospheric correction and crosstalk correction (www.lpdaac.usgs.gov).

3.1.3. Aqua MODIS calibrated radiance 5-min L1B swath 1km night thermal images

MODIS collects information within 36 spectral bands. Bands from 20 to 36 belong to thermal infrared region (Table 3.2).

Table 3.2: MODIS band details of thermal region (http://modis.gsfc.nasa.gov/about/n)

Primary Use	Band	Wavelength (μm)
Surface/Cloud Temperature	20	3.660 - 3.840
	21	3.929 - 3.989
	22	3.929 - 3.989
	23	4.020 - 4.080
Atmospheric Temperature	24	4.433 - 4.498
	25	4.482 - 4.549
Cirrus Clouds Water Vapour	26	1.360 - 1.390
	27	6.535 - 6.895
	28	7.175 - 7.475
Cloud Properties	29	8.400 - 8.700
Ozone	30	9.580 - 9.880
Surface/Cloud Temperature	31	10.780 - 11.280
	32	11.770 - 12.270
Cloud Top Altitude	33	13.185 - 13.485
	34	13.485 - 13.785
	35	13.785 - 14.085
	36	14.085 - 14.385

MODIS satellite sensors have been mounted on two platforms called terra and aqua. Aqua moves form south to north twice a day and it passed equator in the afternoon.. (Savtchenko et al., 2004).The images which were acquired around 3am were available for the study area. The predawn scenes are productive in

identifying hotspots as surrounding materials which has heated up at day has enough time to cool down (Hecker et al., 2007).

MODIS Aqua Calibrated radiance images with 1km resolution data was downloaded using the Warehouse Inventory Search Tool (WIST) of NASA data depository (https://wist.echo.nasa.gov/api/). Cloud free images within the dry season of the area were the searching criteria. The cloud free images were selected using the cloud free day time images in the same day suggesting that that the night image will also have less cloud cover. Dry season images were selected so as to have less moisture contents. Only the images where the study are falls in the middle of the very wide swath (2300km) was selected to prevent from the distortions at the edge of the images. Two images from two different days were used for the analysis. The information of the two MODIS scenes used are shown in the table 3.3.

Table 3.3: Details of two MODIS images used in the study

	Date	Acquisition Start time (GMT)	Acquisition Stop time (Local)	Centre point	
				Latitudes	Longitudes
01	06/07/2010	23:40	02:40.40 (07/07/2010)	5.4252’	29.4083’
02	15/12/2010	23:30	02:35:40 (15/12/2010)	5.5998’	29.8228’

3.1.4. Legacy data

Secondary data was received from the Geological survey of Uganda and rest was collected from articles which were written on the studies on Buranga area.

1. Hot spring locations

The hot spring locations were acquired from the literature and confirmed the coordinates of the location using Google earth.

2. Geological information

The 1:250,000 geological map of Fort Portal, Uganda developed by the Geological survey of Uganda was used for the validation and verification of results. Known mineral occurrences were from the Secondary data received from the Geological survey of Uganda.

2. Land use

These data was extracted from Secondary data received from the Geological survey of Uganda.

3. Subsurface warm body location

This data was extracted from (Ochmann, et al., 2010; Rumpker et al., 2007). All the P wave anomaly tomographic model depth profiles (Figure 2.7) geo-referenced in to WGS 1984 UTM Zone 35N. The 3D tomographic profile in 10km depth was digitized to overlay with resulted images from image analysis.

3.2. Methodology

The methods which were followed based on the objectives and the available data show in the Figure 3.1.

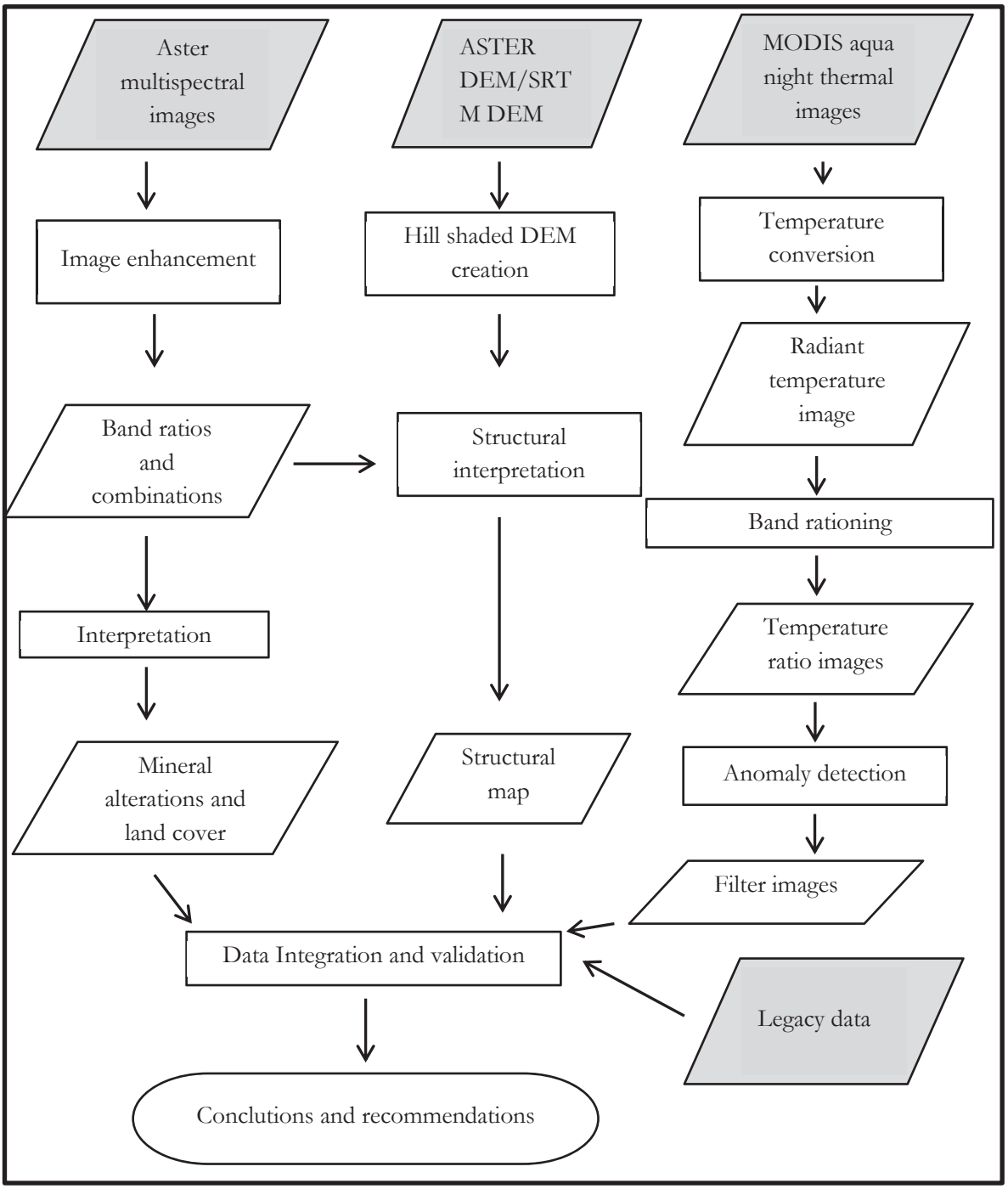

Figure 3.1: Methodology flow diagram

3.2.1. Processing of ASTER multispectral bands

ASTER multispectral data was used for the mapping mineral alterations. Three scene of ASTER AST_ 07XT Surface Reflectance data of VNIR & Crosstalk Corrected SWIR bands and AST_L1B Registered Radiance at the Sensor TIR bands were used for the analysis. All the bands were resamples in to 15m because the involving bands should be in the same spatial resolution to create band combinations and ratios. The TIR band of the L1B data was atmospherically corrected by the ENVI Thermal Atm correction tool. Then these three scenes were mosaic together. A stripe which is with null values at the

western side of the images running NNE was resulted due to the mosaic. As the band ratios and band combinations does not consider the statistics of the whole image this stripe was neglected.

3.2.2. Mapping vegetation and surface land cover

The Buranga area has partly dense vegetation and partly covered with sparse vegetation (Natukunda, 2010). This can hinder the mapping of surficial minerals using the satellite images. Before making the mineral alteration map, a land cover map was produced using ASTER imagery. The NDVI image was created using reflectance values of aster bands 3(NIR) and 2(Red). Values of the NDVI indicate the amount of green vegetation. As known the green vegetation reflects mostly NIR region and absorb the red at the visible region (Figure 3.2). This sudden change at visible and NIR region is called red edge position (Horler et al., 1983).

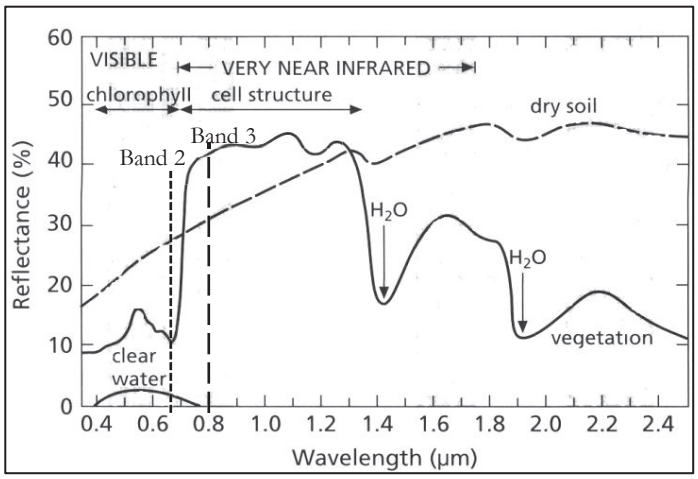

Figure 3.2: The typical spectral reflectance curve of vegetation, dry soil and water (Drury, 2001)

The NDVI equation (equation 1) consider the red edge effect and improves the values at the NIR region and delineates the green vegetation in high values (Wang et al., 2004). With reference to the spectral characteristics shown in the Figure 3.2 the dry soil gets the intermediate NDVI values and clear water gets the lowest.

NDVI= (Reflectance NIR-Reflectance Red)/ (Reflectance NIR+ Reflectance Red) ----------1

The high dense vegetation values were further confirmed by comparing with the red colour of the ASTER band combination 3:2:1. This false colour combination shows the NIR band in RED. Therefore vegetation appears in red hue.

After inspection of different band combinations of ASTER imagery, the band combination 5:4:7 was also used to discriminate the different land cover types.

The resulted NDVI image gave values from -1 to 1. The high values were over the densely vegetated area. By visual observation comparing with Bands 3:2:1, the dense vegetation values seems to falls within 0.62 to 1. Within the dense vegetation, there are two classed which could be identified using the band combination 3:2:1 and 5:4:7. Hence the densely vegetated area was divided into two classes ranging from 0.62 to 0.75 and 0.75 to 1. The open areas were classified from 0.27 to 0.62. The values less than 0.27

match with the pixel values on water bodies. The open areas from 0.27 to 0.62 were further classified with relation to the other band combinations depending on the variation of tone. mineral alteration mapping

3.2.3. Mapping mineral alterations

Analysis of ASTER images will support discrimination of different types of minerals. The characteristic hydrothermal alteration minerals due to geothermal activities (e.g., alunite , illite, kaolinite, chlorite) shows prominent Al-OH absorption features within the wavelength range of 2.1μm to 2.3 μm due to the vibrational processes of Al-OH and Mg-OH bonding (Clark et al., 1990). Therefore those alteration minerals, if any, can be differentiated using ASTER images of short wave infrared (SWIR) region (Gozzard, 2006). TIR can be used to differentiate quartz, carbonate and amphiboles (Gozzard, 2006). The hot spring indication mineral, travertine, is spectrally detectable using the spectral carbonate absorption features (around 2.3 μm in SWIR and 11.5 μm in TIR) of the mineral (Jones et al., 2010), (Rockwell et al., 2008). On the basis of the absorption position of particular minerals and the wavelength range of the particular bands, band combinations and band ratios can be created to discriminate minerals (Hewson et al., 2005).

The main purpose of this processing was to identify the alteration minerals due to geothermal activies in the study area. The pixels values for the dense vegetation were utilized for the masking vegetation while mapping the mineral alteration due to the geothermal activities. Before creation of any band ratios all the bands were masked for the vegetation where the NDVI value is higher than 0.65.

Phyllic, argillic and silicification alteration are expected in geothermal systems (Kühn, 2004). The lithology around the area shows mostly the basement gneissic rocks. Hence the prophyllitic alterations overprinting the ferromagnesian bearing rocks cannot be expected

ASTER band combinations were used to identify the Al-OH minerals which are the products of the phyllic and argillic alterations. The band ratio (B5+B7)/B6 was created for the discrimination of the Al-OH group content as shown by (Cudahy, 2011). The values of resulted ratio image ranged from 0.0 to 0.038. The value at 90% percentile of cumulative which is 0.012 was considered as the threshold. The pixel values higher than 0.012 define the Al-OH containing minerals.

Ochmann et al. .(2008) has mentioned that in drilling of shallow exploration well in this area has evidenced the formation of carbonates in the fault breccia. Hence the band ratio (B6+B9)/(B7+B8) was created for the discrimination of the Mg-OH group contest as shown in the (Cudahy, 2011). This band ratio mainly identifies the carbonates. For the Mg-OH band ratios the values shows as the 0.0 to 1535. The value at 90% percentile of cumulative was considered as the threshold. The pixel values higher than 333 consider to be the area with Mg-OH containing minerals.

Kratt et al. (2006) has found occurrence of gypsum at the Brady–Desert Peak geothermal fields, Nevada which is an extensional type geothermal system. The gypsum is formed at the geothermal systems due to the sulphur content in the geothermal fluids. The known mineral occurrence of gypsum is visible north to the Ruwenzori Mountain. Therefore for verification of occurrence of gypsum as a result of geothermal activity, band ratio B5/B4 was applied (Shi et al., 2010). The ratio values gave the ranges form 0 – 2.43. The value at 90% percentile of cumulative which is 0.65 was considered as the threshold.

The threshold values which has been suggested by Cudahy (2011) is different from the threshold that was used in this study. Cudahy (2011) has used the ASTER L1B radiance at sensor images with cross talk correction while I used the reflectance images. He has mentioned that the reflectance imagery can also

exhibit the mineral content with these specific band ratios. Further, the threshold values which have been given in his study can vary in different environment.

Above ratio were firstly visualized in to a colour range and the high values showed clustering within some areas. The resulted images after threshold agreed with the clustering areas. The known mineral occurrences were used to validate the results.

The band combinations B11/ (b10+12) for the identification of the quartz was applied to find any silicification (Cudahy, 2011). However the resulted image did not give a result which can be interpreted to show an area which shows silicification. The resulted images showed a sugary texture and applying a threshold was problematic.

3.2.4. Identification of thermal anomalies

In this study, night thermal images were utilized to map the surface thermal anomalies due to geothermal heating. Night thermal infrared images have been used in several instances to detect thermal anomalies associated with geothermal activities (Calvin et al., 2002);(Eneva, et al., 2006);(Pastor, 2010). Owing to the high cloud content in the available ASTER night thermal images of the area, MODIS aqua calibrated radiance night thermal images were used to identify the areas with elevated temperature.

The bands from Bands 20 to band 36 (except 26) which is in the TIR region were used for the study. Among 16 bands, 21, 24, 25, 27, 28, 30, 36 showed strong EW stripping effects. Hence the images were de-stripped using the ENVI and HypPy software. The de-stripping divide method in the HypPy programme gave the optimum reduction of the stripping effect. Therefore the resulted images from de-stripping divide method in HypPy programme was used for further analysis. Afterward, images were geo-referenced using the MODIS geolocation images (MYD03). De-stripping was practiced before the geo-referencing for the reason that geo-referencing rotates the imagery and makes de-stripping in a second step useless.

When considering the statistics of the images, in both scenes, the Band 29, 31 and 32 shows comparatively higher radiance as the earth targets radiates highest energy around 10 microns. (Figure 3.3). The band 24 and 25 shows comparatively higher atmospheric absorption. Because of that the band 24 and 25 was not considered in further analysis.

The DN values of thermal images can be used to calculate the surface temperature. Therefore the approximate temperature of the thermal anomalies can be deduced using the brightness of the map.(Abrams et al., 2002);(Coll et al., 2007). As the images were in the radiance values, the values were converted to temperature values to get an idea about the temperature variation over the area.

The raw radiance values were converted to the radiant/brightness temperature images using ENVI software together with ASTERrad2bright IDL. This IDL uses the inverted Plank's radiance function to convert radiance to brightness temperature. The central wavelength of the band is considered in the calculations. The pixel values of the resulted images displayed temperature values in Kelvin. The radiant temperature images were also de-striped and geo-referenced in accordance with the above mentioned way.

The earth's surface does not act as a true blackbody. Hence the DN values of thermal images do not represent the actual temperature. The radiant/brightness temperature is always less than kinetic temperature of a material. (Lillesand et al., 2004). The materials with high emissivity give less brightness

temperature values. That is the materials with same kinetic temperature and with different emissivity give different brightness temperature values. The emissivity of the materials was not considered in the calculations.

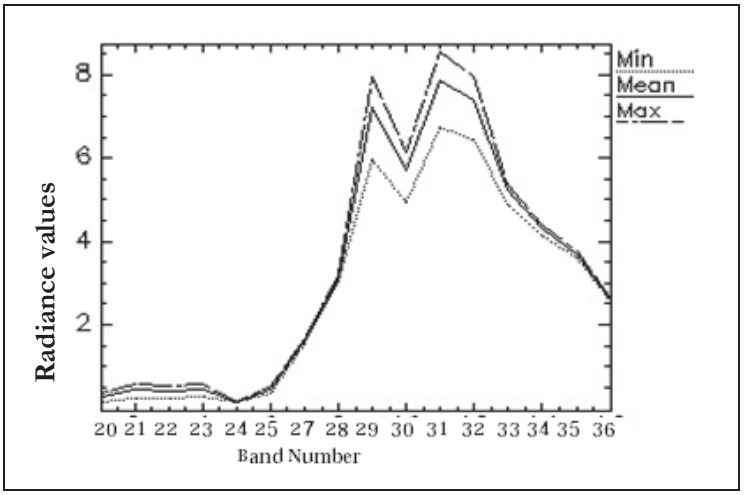

Figure 3.3: Spectra of MODIS aqua Radiance images (06th of July, 2010)

Radian temperature or brightness temperature doesn't give the actual or kinetic temperature of a material.

A small hot spot within a 1km pixel of background temperature cannot be identified directly using the pixel size of 1km. The temperature variation within the pixel is averaged in to a one value and the difference between background become very less. Therefore the sub pixel size hot spot identification method was used to enhance the thermal anomalies less than 1km (Hecker, et al., 2007). The sub pixel size hot spot identification is based on the displacement law of Wien and Plank's law (Dozier, 1981).

The temperature of the pure pixels remains constant and the mix pixels temperature vary with the wavelength of electromagnetic spectrum depending on the contribution of each material (Dozier, 1981). Hence in band ratios of two wavelengths, ratio value of pure pixels gets the values of 1 and the ratio value of mix pixels will take the values less or higher than 1. The pixels with hot spot must give higher values than pure pixels while the low wavelength band is divided by high wavelength band.

According to the Wien's displacement law the radiant energy peak at a certain wavelength shifted to the shorter wavelength with the increasing of kinetic temperature of an object. Following Wein's displacement equation (Equation 2) can be used to calculate the responsible wavelength for a certain radiant peak temperature.

$$\lambda \max = b/Trad \quad \text{---------} \quad 2$$

λ max refers to the peak wavelength (in meters) which is responsible for the radiant temperature (in Kelvin) which is shown as T. b is Wien's displacement constant of 2.8977685(51)×10−3 m·K (Lillesand, et al., 2004)

The possible radiant temperatures for the wavelength vales of the MODIS thermal bands were calculated using the Weins displacement equation (Table 3.4). For the band ratios the radiant temperature at different bands were considered

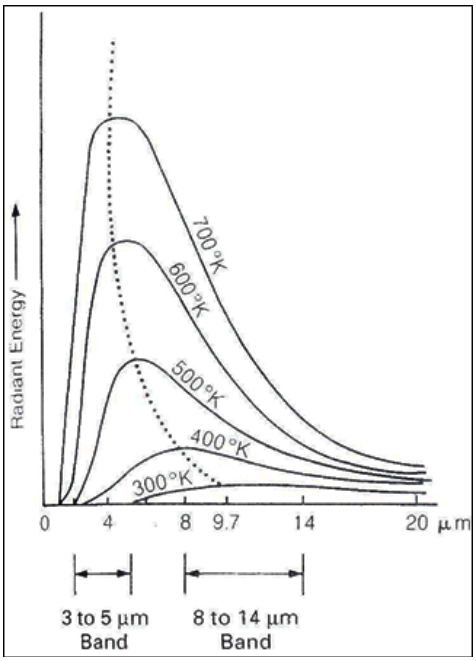

Figure 3.4: The energy radiation distribution at different temperatures (Lillesand, et al., 2004)

Table 3.4: The radiant temperature values for the wavelength values of the different MODIS bands based on Wein's displacement law

Band No	Wavelength (µm)	Average wavelength(µm)	T (Kelvin)	T (Celsius)
20	3.660 - 3.840	3.75	773	500
21	3.929 - 3.989	3.959	732	459
22	3.929 - 3.989	3.959	732	459
23	4.020 - 4.080	4.05	715	442
24	4.433 - 4.498	4.4655	649	376
25	4.482 - 4.549	4.5155	642	369
27	6.535 - 6.895	6.715	431	158
28	7.175 - 7.475	7.325	395	122
29	8.400 - 8.700	8.55	339	66
30	9.580 - 9.880	9.73	298	25
31	10.780 - 11.280	11.03	263	-10
32	11.770 - 12.270	12.02	241	-32
33	13.185 - 13.485	13.335	217	-56
34	13.485 - 13.785	13.635	212	-61
35	73.785 - 14.085	13.935	208	-65
36	14.085 - 14.385	14.235	204	-69

The surface temperatures of Buranga hot springs are about 98^{0}C (Bahati, 2004). For 95^{0}C radiant temperature, the wavelength value is 7.89 μm which is comparable with the MODIS band 28 and 29 (Table 3.4). The temperature of the Ruwenzori Mountain is about 25^{0}C. The wavelength value for this temperature is comparable with the MODIS band 30. As the band 28 shows higher atmospheric absorption than the band 29 (Figure 3.5), band 29 was used to represent the hot spring temperature values (table 3.4). However even the band 30 is showing the higher atmospheric absorption (due to ozone absorption peak at 9.6 μm) than the band 31 and 32. Therefore band 31 was used instead of 30. For that reason the band ratio of 29/31 was prepared at first. As the 31/29 did not give much variation in the ratio values the instead of band 29 one of the bands from 20 to 23 was selected. As band 22 was close to the band 28 and has lower atmospheric absorption the band ratio 22/ 31 was selected for the identification of the pixels with hot spots. Consistent with the sub pixel size hot spot identification theory the low wavelength bands were divided by the high wavelength bands. The ratio values higher than 1 specifies the pixels with the hot spots higher than the background values.

The resulted ratio images were inspected visually for the identification areas with hot spots. And also the resulted ratio images were classified using the hotspot detection algorithm which is shown in Zhang et al. (2004). This method identifies the pixels with hot spots comparing with the neighbouring pixels. This algorithm calculate the histogram within a kernel while moving along the image. The first minimum after the global Maximus is considered as the margin to differentiate pixels with anomalous values from background values. This show the pixels which are standing out as anomalous within a homogeneous background. The final result will be the image with percentage of all positive anomaly pixels for the each kernel size. This method the Checking the resulted images from kernel size 11*11 to 35*35, the images from filtered with 11*11 was used for the analysis. The pixels with value more than 70% were considered as the pixels with anomalous temperature values.

3.2.5. Surface structural Interpretation

The spatial distribution and geometry of structural features will allow detection of the association of the geothermal source to thermal anomalies and the surface mineralogy. Basically, different data sets and different methods were used to enhance and extract geological structures of the area.

SRTM DEM with 90m resolution and the ASTER new version DEM with 30m resolution were mainly used to extract the surface structures. The one directional and three directional shaded relief of both DEM were prepared. Shaded relief image of DEM data improves the elevation change within a terrain using azimuth and altitude angles of Sun and hence the morphology change is highlighted. The resulting illumination and shadow effects were useful in identifying the directions of slopes. One directional shaded relief map was prepared using ARC map software with different illumination azimuth and elevation angles. For the processing, the default values azimuth angle was 315^0 and default elevation angle was 45^0. When the azimuth angle and elevation angle changed the brightness of the image varies and lacks the clarity of the image. At some instances it gave the inverted elevations as valley seems like highly elevated than mountains as the eye is practiced to expect illumination in NW direction. There for the images prepared with the default values were selected for the analysis. Besides three directional shaded relief maps of ASTER and SRTM DEM were created using ILWIS software. This method makes three shaded relief images considering three directions and then formulates the colour composite of three of them followed by 5% linear stretching. The three directions are west, north-west and north (ILWIS, 2007).

As suggested by Gozzard (2006), the aster image combination of band 7:4:2 was also used in the interpretation of structures. The ASTER 15m resolved band 2 was filtered using directional convolution

filter with 3*3 kernel size (Pirasteh, 2011). The directional filtering is an edge enhancement method (Paplinski, 1998). In edge enhancement method it detects considerably high difference between adjacent pixels. In directional filtering it calculates the first derivative of the given direction. The directional filtering was done in different directions (0^0, 45^0, 90^0, 135^0, 180^0, 225^0, 270^0, 315^0) as with reference to Koehn, et al. (2008) the main structural features are trending along different directions like NS, EW and NW. As there was no any visible difference of images with different filter directions, one of them was used for the analysis.

Major and minor lineaments were classified depending on the visibility of the linear features on the resulted hill shaded DEMs. The lineaments which were visible at the scale of 1:500, 000 was classified as the major lineaments .The lineaments which were only visible at the scale of the 1: 100, 000 were classified as minor lineaments. Two dimensional topographic profile graphs were drawn perpendicular to the fault lines so as to identify the slope geometries like direction and approximate angles. The topographic profiles indicate the elevation variation along a certain distance on the surface. The study area is consist of horst and graben structure demarcated by steeply dipping normal faults (D. Koehn, et al., 2010). The major lineaments which fall between a high elevation differences which show horst and graben structures on the topographic cross sections were classified as the major faults.

The rose diagram was drawn for the recognition of the lineament pattern with reference to the directions. The rose diagrams are capable of summering the linear patterns with the direction and frequency of distribution (Nemec, 1988).

3.2.6. Data Integration

The results structural interpretation, mineral alterations, known geothermal hot springs and the information extracted from the P wave velocity anomaly tomographic model from Ochmann et al. (2010) were used in data integration. The data were link together to identify the association of the surface structures and the surface heat source. A vertical profile graph till depth of 10km was created along a line which is cross cutting the hot spring locations, related structures and subsurface heat source.

4. RESULTS AND DISCUSSION

This chapter includes the results on the mapping alteration mineral and land cover, identification of thermal anomalies, surface structural interpretation, and their relation to the geothermal manifestation of the Buranga area. The Buranga hot spring location will be plotted on the resulted image as the known surface geothermal expression.

4.1. Vegetation and land cover mapping

Using only an NDVI image, it is difficult to distinguish different type of vegetation cover in the area. The tone of the other ASTER band combinations is useful in differentiating land cover together with the NDVI image (Figure 4.1). The Ruwenzori mountain and the Semuliki National Park area show the highest NDVI values. With comparing to the ASTER 4:5:7 and 3:2:1 (Figure 4.1;(a) and (B)) the threshold for the densely vegetated area in the NDVI image could be determined as 0.65. The area is having very little exposure of bare soil or rocks. The open sediment cover is shown in magenta colour in the Band ratio 5:4:7. And cyan in 3:2:1. Only these areas can give any kind of spectral signatures of mineral in the area. The land cover units interpreted based on these observations are shown in the Figure 4.2.

In relation to the classified images of the NDVI image (Figure 4.4), the hot spring locations are plotted on the area where on the open areas within the densely vegetated terrain. As per to the exiting land cover of the area prepared by the geological survey of Uganda, this area is called as degraded forest (Figure 2.2). The forest degradation may be due to the thermally stressed vegetation. But it could not be differentiate using the ASTER multispectral data. The spectral characteristic of the vegetation must be collected using the field spectral measurement for further classification of the vegetation using remote sensing methods. By that way, the identification of the geothermal potential area using the geo-botanical characteristics (thermally stressed vegetation) can be applied. The other areas of sediments within the dense vegetation on rift valley_1 (figure 4.5) (west side of the Ruwenzori Mountain), may have been caused by the marshy environment or by hot water lakes within densely vegetated vegetation. These areas also have to be verified with the field investigations.

The interpretation of the different land cover units (Figure 4.2) is also useful in the mineral alteration mapping and in justifying the temperature variation of the area.

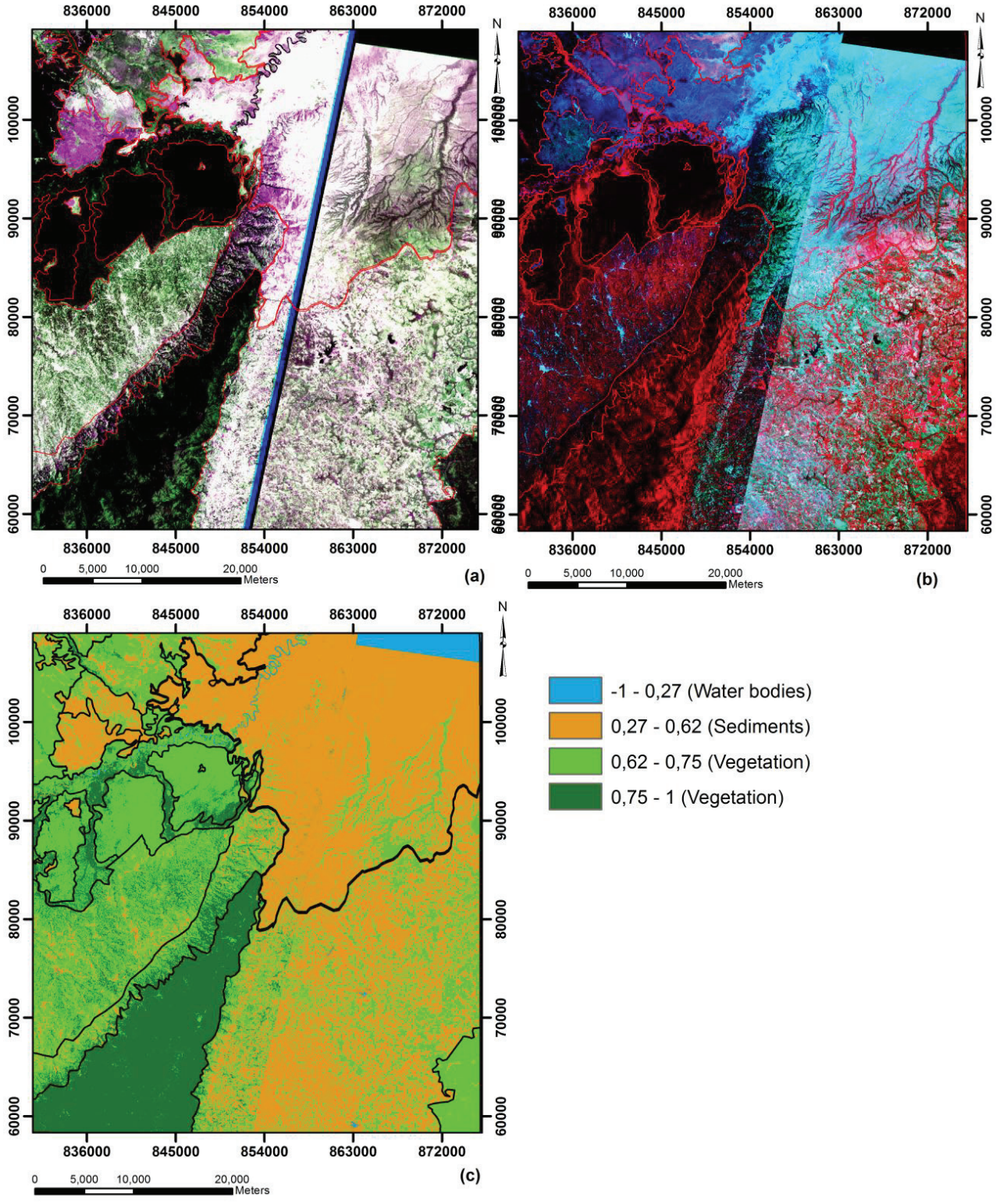

Figure 4.1: (a) ASTER band combination 5:4:7 (a) ASTER band combination 3:2:1 (c) Classified NDVI image (The boundaries of land cover which was interpretated using ASTER imagery are overlain on the images)

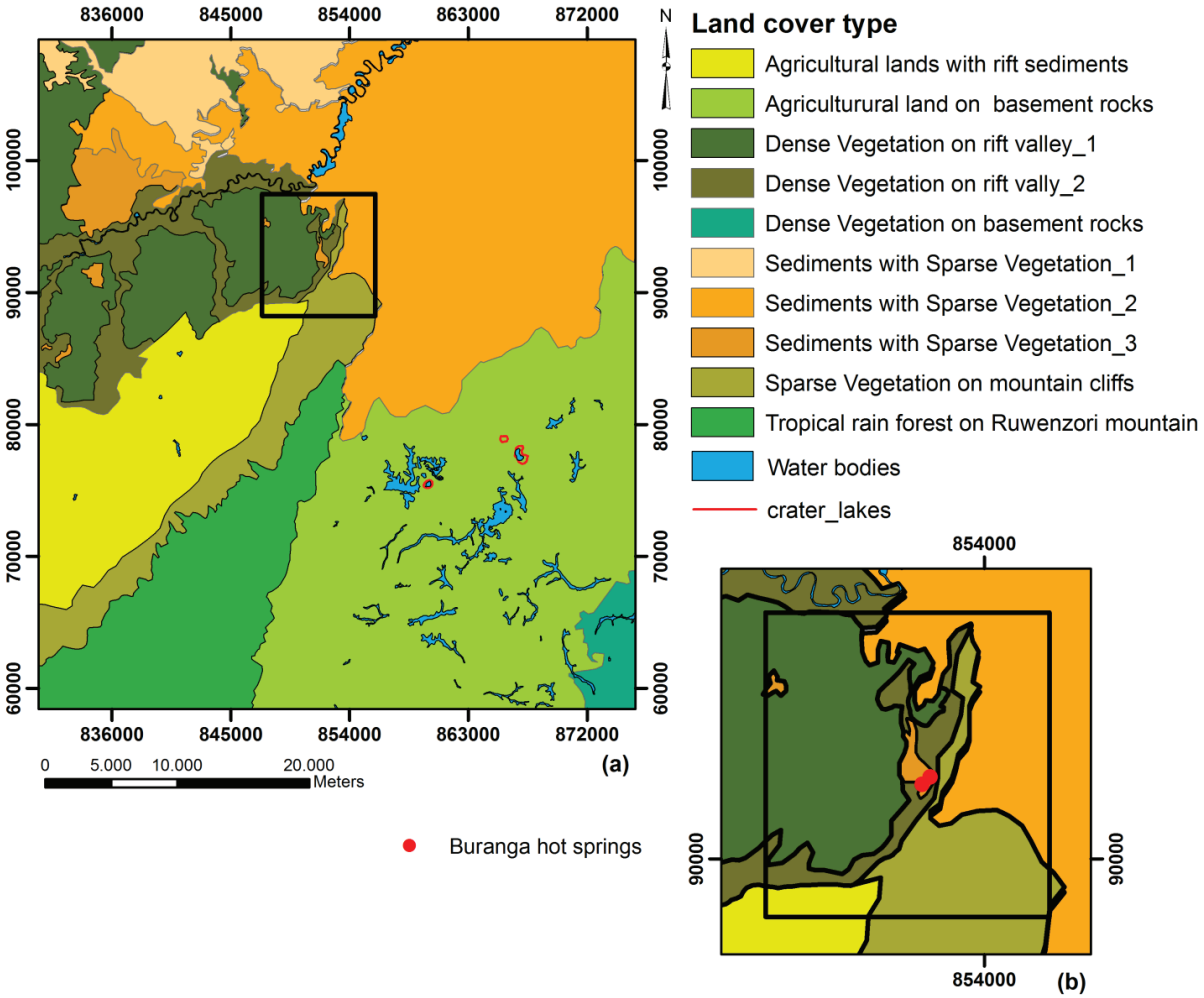

Figure 4.2: Land cover of the area interpreted using ASTER imageries

4.2. Mappin mineral alterations

The resulted images for Mg-OH, Al-OH containing minerals and gypsum show clustering in different regions (Figure 4.3 and 4.4). Comparing the distribution of the Al-OH, Mg-OH containing minerals map, they do not correlate with each other. However the Mg-OH content map and gypsum maps show similar spread at most areas. The mineral content above the threshold values are presented in red on the original ratio images.

Looking at the area with the known hot spring location (Figure 4.3 (b); (d) and figure 4.4 (b), few areas with Al-OH containing minerals occurrence is visible. Rift sediment has been altered due to the effect of the geothermal water or weathering of feldspar bearing basement gneisses. This has to be confirmed with further studies. The identification of the mineral alterations around the Buranga hot springs is hindered by the surrounding dense vegetation.

On the availability of the different mineral content over other areas will be discussed in the data integration section (Section 4.4).

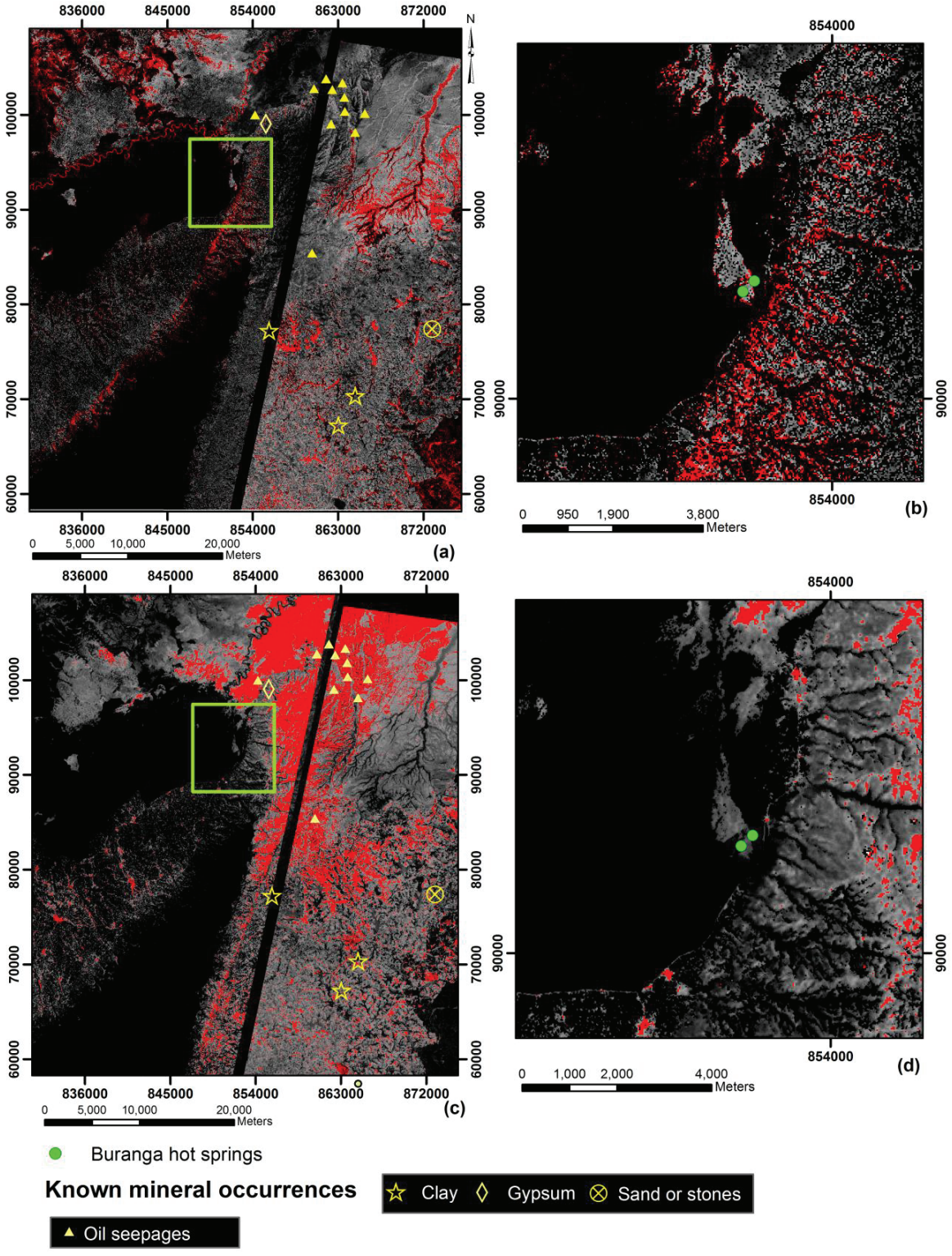

Figure 4.3: (a) Al-OH containing mineral map (b) Al-OH containing mineral map the area around hot springs (c) Mg-OH containing mineral map (d) Mg-OH content map the area around hot springs ((c) and (d) are the zoom images which shown in a green box of image (a) and (b), the mineral occurance shown in red colour))

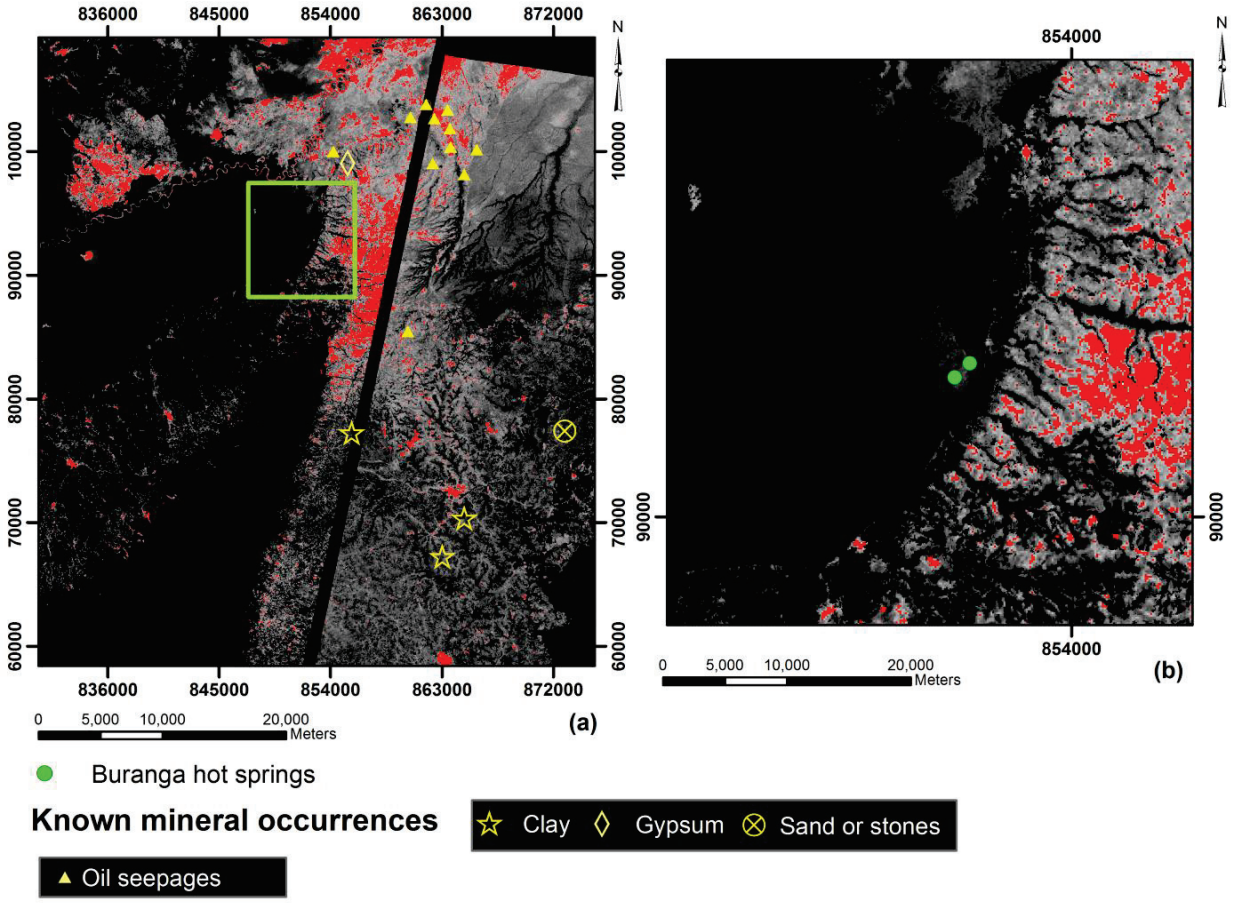

Figure 4.4: (a) Gypsum content map the study area; (b) is the zoom images which shown in a green box of image

4.3. Identification of surface temperature anomalies

In this section the resulted surface temperature variation which was detected through the radiance temperature of Aqua MODIS images and from the sub pixel size hot spot identification method will be discussed with relevant to the known hot spring locations and the other land cover types which were identified in the ASTER multispectral image analysis.

4.3.1. MODIS night thermal Radiant temperature Image analysis

Considering the resulted radiant temperature images, highly vegetated Ruwenzori mountain top area has the lowest temperature values (Figure 4.5). This may have caused by the higher elevation of the mountain. The high elevated terrains are cooler than the low elevated surrounding environment at day and also at night time (Lillesand, et al., 2004). Higher temperature values display on the areas with sediments with less vegetation. These areas are at the western side of the Ruwenzori Mountain and north to it. This is the rift valley zone area. The highest temperature values falls on the bare lands filled with sediments. Hence the rift valley area with less vegetation is having higher temperature values in the MODIS night thermal radiant temperature images. Generally the rocks and soils shows lower radiant temperature at night more than other land cover types like vegetation and water (Figure 4.7). However The water has the high thermal inertia and it absorbed more radiant energy at day time and stay warmer at night than surrounding

(Lillesand, et al., 2004).The water seems brighter at night with comparing to the surrounding. Therefore the areas with bare soil showing highest temperature values may have been caused by the high moisture content and the dense stream network over the sediments of rift valley zone (Figure 4.5).

Accordingly there is an effect of diurnal changes and altitude of the temperature values of the surface land cover types on the surface temperature calculated using the MODIS night thermal images.

The temperature of the pixels over the rift valley zone in December scene is higher than in the June scene (Figure 4.6). Although, December and July falls within the dry season of the area, they may show different weather conditions. The December is having high rainfall than in July (www.climatetemp.info). This may have triggered by the annual changes of the surface land cover like filled water bodies. Hence the annual variation of the characteristics like moisture content of the soil and water content in the streams of the Buranga area has an effect on the temperature value difference in the two scenes.

In both scenes, the radiant temperature of the pixels where the hot spring located gives as the 288 k. (15^0 C). However the highest radiant temperature values of the area are 3-4 degrees higher than that of hot spring areas. Therefore due to the influence of high temperature over moist sediments, it is not possible to classify the areas with elevated temperature due to geothermal activates with the radiant temperature of night thermal MODIS image. And also the low resolution of the MODIS image is not high enough to detect the high temperature values of the hot springs.

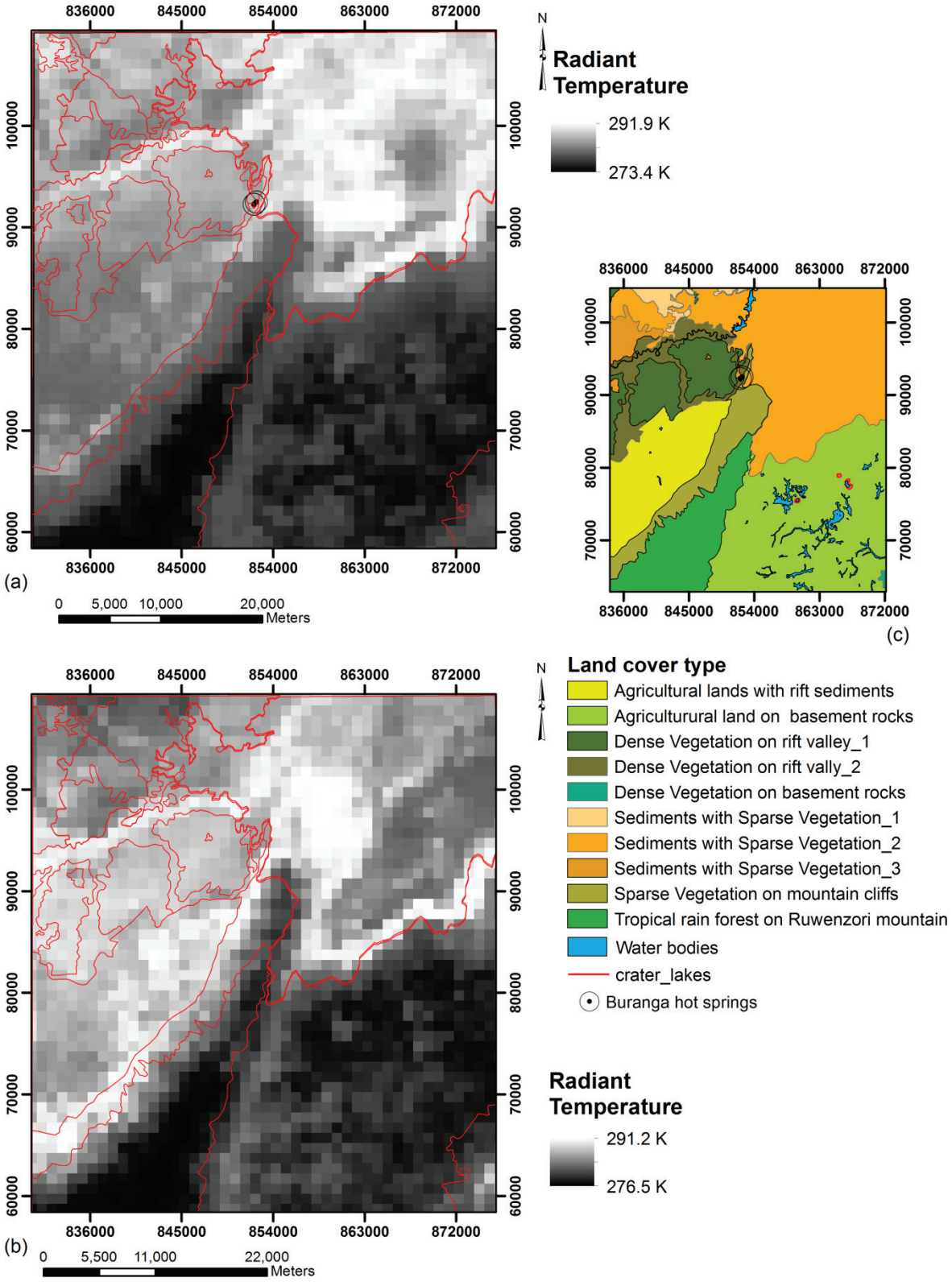

Figure 4.5: (a) Radiant temperature image of MODIS Band 20 of 06th July, 2010 Scene; (b) Radiant temperature image of MODIS Band 20 of 20th December, 2010 Scene (C) Surface land cover types

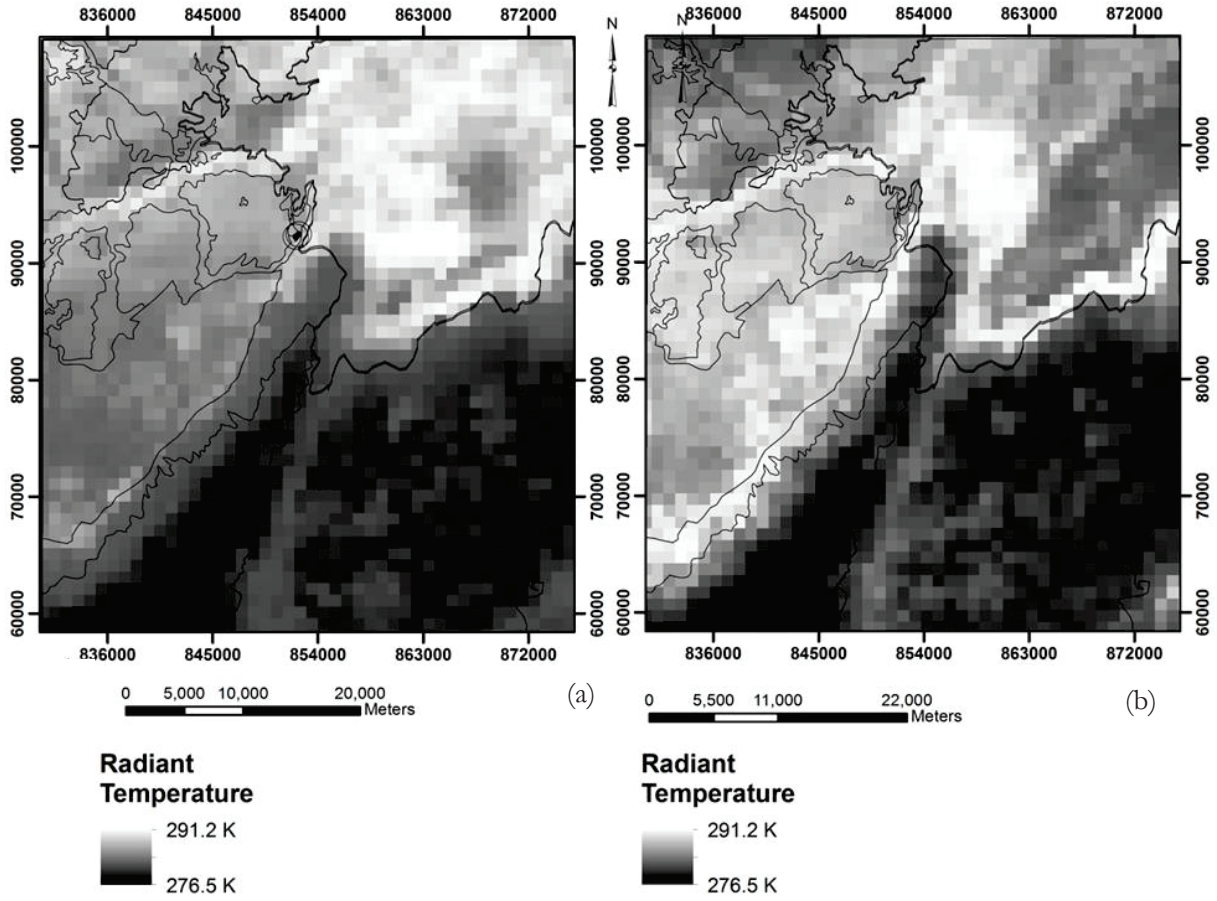

Figure 4.6: (a) Radiant temperature image of MODIS Band 20 of 06th July, 2010 Scene; (b) Radiant temperature image of MODIS Band 20 of 20th December, 2010 Scene stretched in within same temperature ranges of June scene

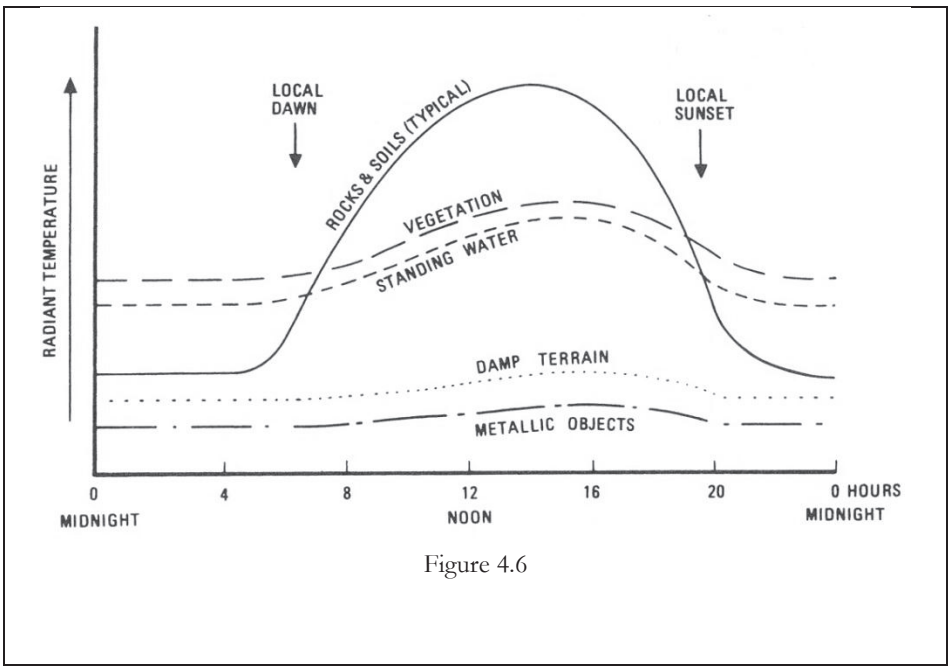

Figure 4.6

Figure 4.7: Typical diurnal variation of radiant temperature of materials (Lillesand, et al., 2004)

Therefore the use of sub pixel size hot spot identification method using radiant temperature values may give a better result than from just only from radiant temperature images.

4.3.2. MODIS night thermal radiant temperature ratio Image analysis

4.3.2.1. Visual Inspection

Due to the lack of information which could be extracted from the radiant temperature images the band ratio of the radiant temperature images were taken into the consideration in identification of surface temperature anomalies related to geothermal heating.

The ratio image 22/31 shows the ratio values ranging form. 0.996 to 1.015 in the July, 2010 image and the values December, 2010 image is ranging from 1.005 to 1.011. Except few pixels in the July-2010 image, all the pixels give values higher than one for the both scenes. This may be because the area is mostly inhomogeneous and gives the values of mix pixels.

The higher ratio values falls on over the sediments with sparse vegetation north to the Ruwenzori Mountain and on Ruwenzori mountain cliffs with sparse vegetation. The sediments with sparse vegetation north to the Ruwenzori Mountain are mixed with dense streams networks, open bare lands and sparse vegetation. Different thermal signatures of these materials within1ikm pixel have given rise to the higher ratio values.
Over the areas which west to the Ruwenzori Mountain and east to it show the low ratio values. This is because these areas are homogeneous with vegetation.

The ratio value from radiant temperature images for the two different scenes from different times don't show much variation.

There are few high ratio values coming out within the low values on the basement rocks with sparse vegetation. They fall within the crater lakes and contribution of some part of lake partially on pixels is visible. The high temperature signature of water at night time (high heat capacity of water) is has given rise to the anomalous ratio values.. There is no enough data to validate this high thermal signature over the lake water is related with gothermal activates or just the effect of high heat capacity of the water.

The resulted ratio values for the areas with geothermal heating coincide by the areas with sparse vegetation. There is no any pixel coming out specifically with high ratio from the area of Buranga hot springs through the background values while visual inspection. Although the results gave an indication about the temperature variation over the area, this method using the MODIS night thermal images are not that productive in visual inspection of the thermal anomalies due to the geothermal activities

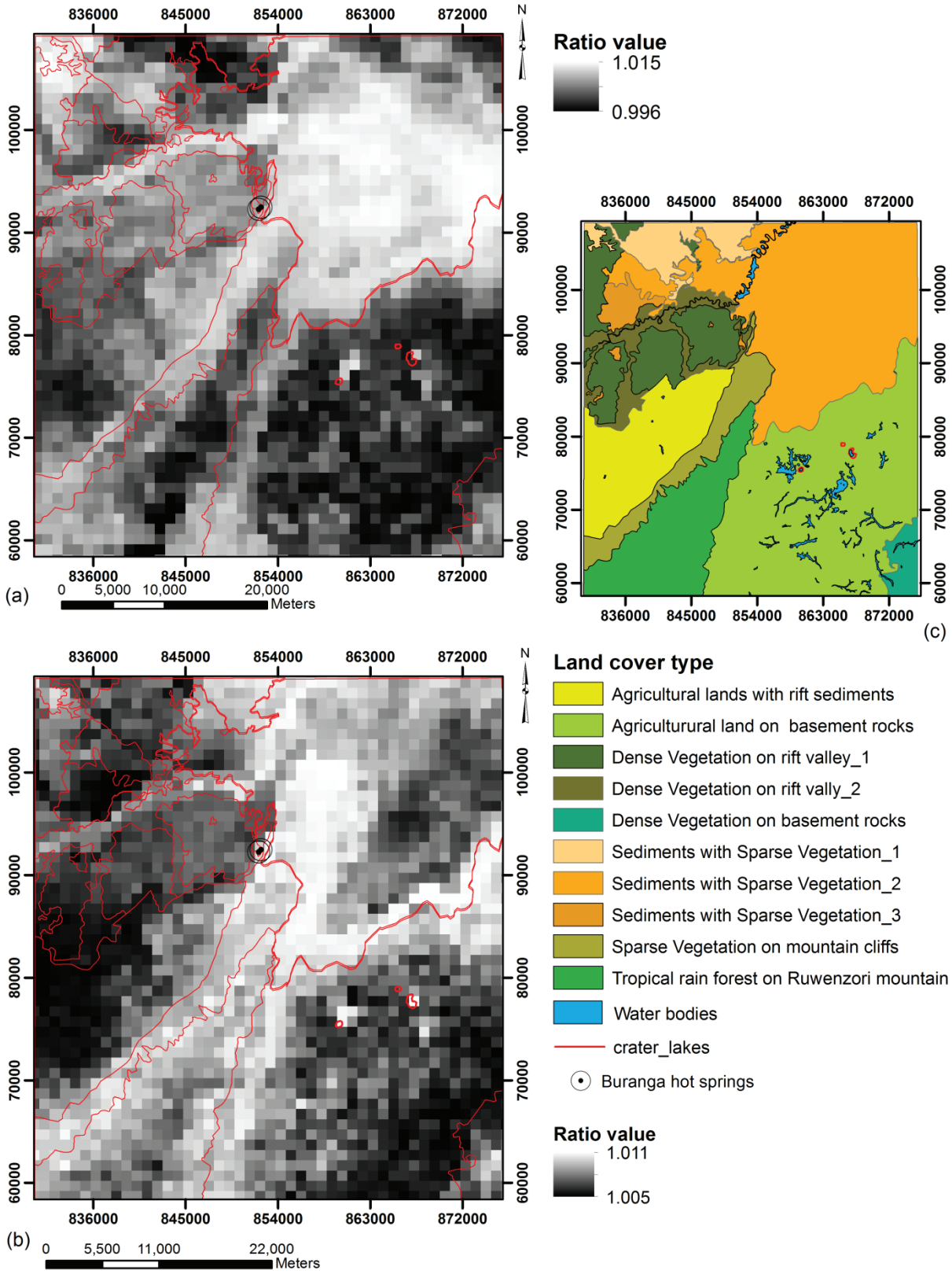

Figure 4.8: (a) Band Ratio 22/31 of Radiant temperature image of MODIS scene 06th July, 2010 Scene; (b) Band Ratio 22/31 of Radiant temperature image of MODIS scene of 20th December, 2010 Scene (C) Surface land cover types

4.3.2.2. Threshold using the hotspot identification algorithm

As all the ratio values are higher than 1, it is difficult to threshold the values depending on the logic that pixels with values higher than 1 have a hot spot inside the pixel. The images resulting from the hotspot identification algorithm could emphasize few pixels which are having higher percentage values. In the image of July-2010, three pixels were highlighted as having values over 70% which considered as the pixels with anomalous values (Figure4.9). The pixel named 1 and 2 are plotting on the sediment cover and there was no any significant feature could be identified relevant to that visible in the aster images or in Google earth. The pixel named in number 3 has been highlighted due to the crater lakes within on basement rocks. This is related to the high temperature values of water at night time. Even the no 6 also highlighted due to the same reason. No 4 also running along the braided river. No 5 plotted on an open mountain cliff. The number 1 and 2 must be investigated further more with field verification for it to be highlighted as a hotspot.

The results from the scene December, 2010 have highlighted hotspots locations different form the scene July, 2010 (Figure4.10). There are two spots higher than the 70%. Number 1 falls on the northern part of the Ruwenzori Mountain and it is having bare lands with sparse vegetation. Even the No 2 is on the Ruwenzori mountain top and no any clue about how this spot has become so specific. The pixels having values from the 50-70% are related with the high temperature signature of water.

The pixels which contain known hot spring locations are not giving high values from the resulted filtered images. At night, the moisture content and dense vegetation has high temperature signature due to the leaf moisture content (Lillesand, et al., 2004). The area with Buranga hot spring is covered with dense vegetated. Therefore, the high temperature signature of the hot spring locations is hidden within the high temperature signature of the dense vegetation.

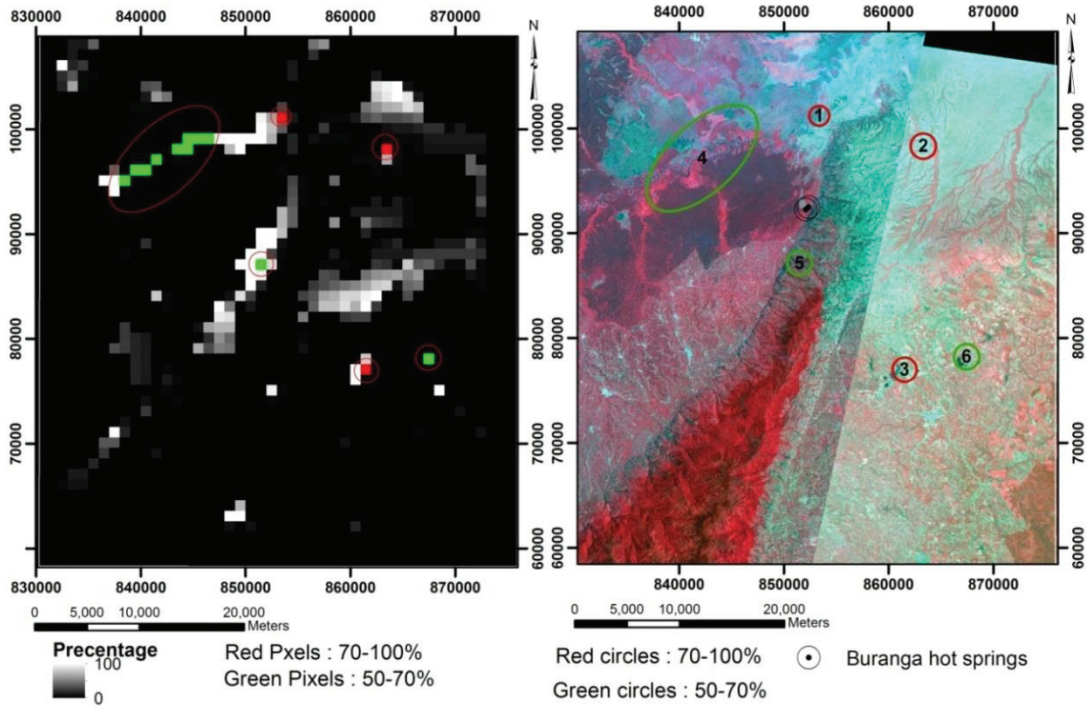

Figure 4.9: Filter image of Band Ratio 22/31 of Radiant temperature image of MODIS scene July, 2010 (left); Anomalous hotspot areas on the ASTER 3:2:1 colour composite (right)

MODIS night thermal images are not strong enough to extract information on the temperature anomalies responsible for the geothermal activities in this area. The low resolution of the images, the inhomogeneity

of the surface cover and high moisture content hinder the enhancing of hotspots. The pixels which contain the known hot spring locations do not give high values from the resulted filtered images

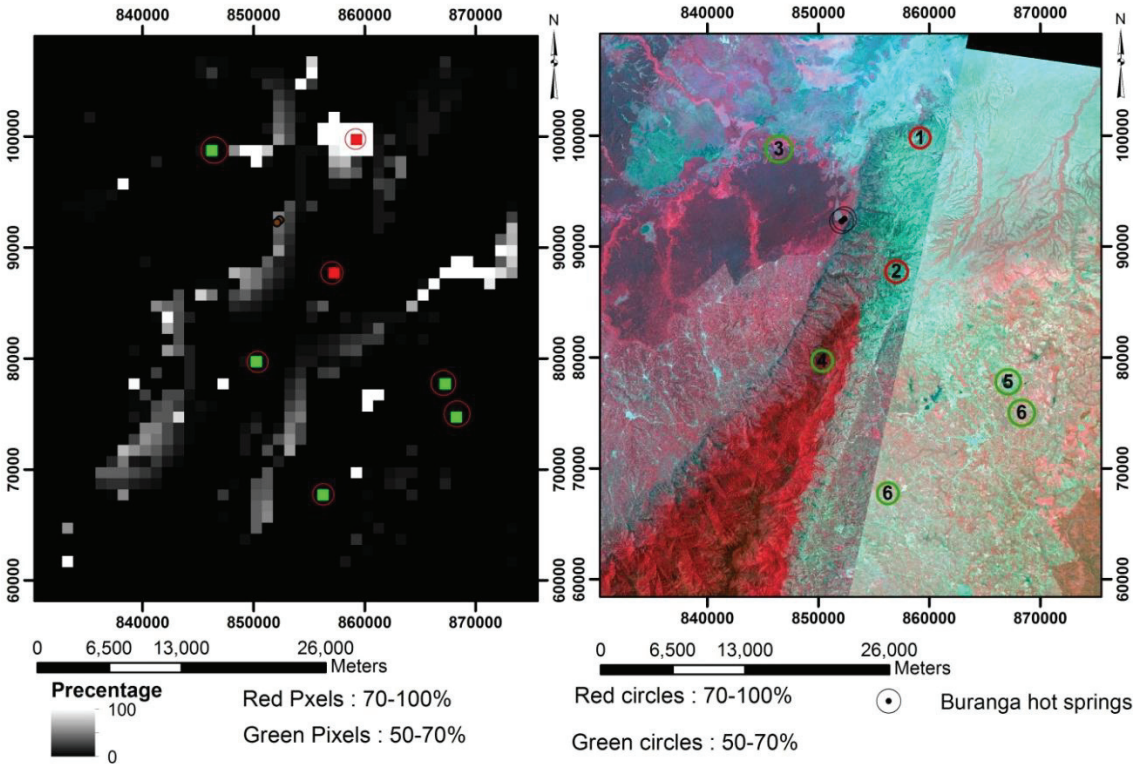

Figure 4.10: Filter image of Band Ratio 22/31 of Radiant temperature image of MODIS scene December, 2010 (left); Anomalous hotspot areas on the ASTER 3:2:1 colour composite (right)

4.4. Surface Structural Interpretation

The structural map was created to understand the relation between geothermal manifestations, subsurface hot body to the geological structures of the area.

According to the results, almost all the hill shaded maps are capable of showing the terrain elevation differences over the study area (Figure 4.10). However, ASTER 30 m data shows more detail than in the SRTM data because of the higher resolution. Hence the ASTER three directional hill shaded DEM

Further the ASTER band 2 with directional filtering could enhance structures which is not clearly visible on the ASTER three directional hill shaded DEM (Figure 4.11). As the ASTER band 2 with directional filtering image is not clear in the scale of the hill shaded DEM, small region of the study area has been enlarged in the Figure 4.11.

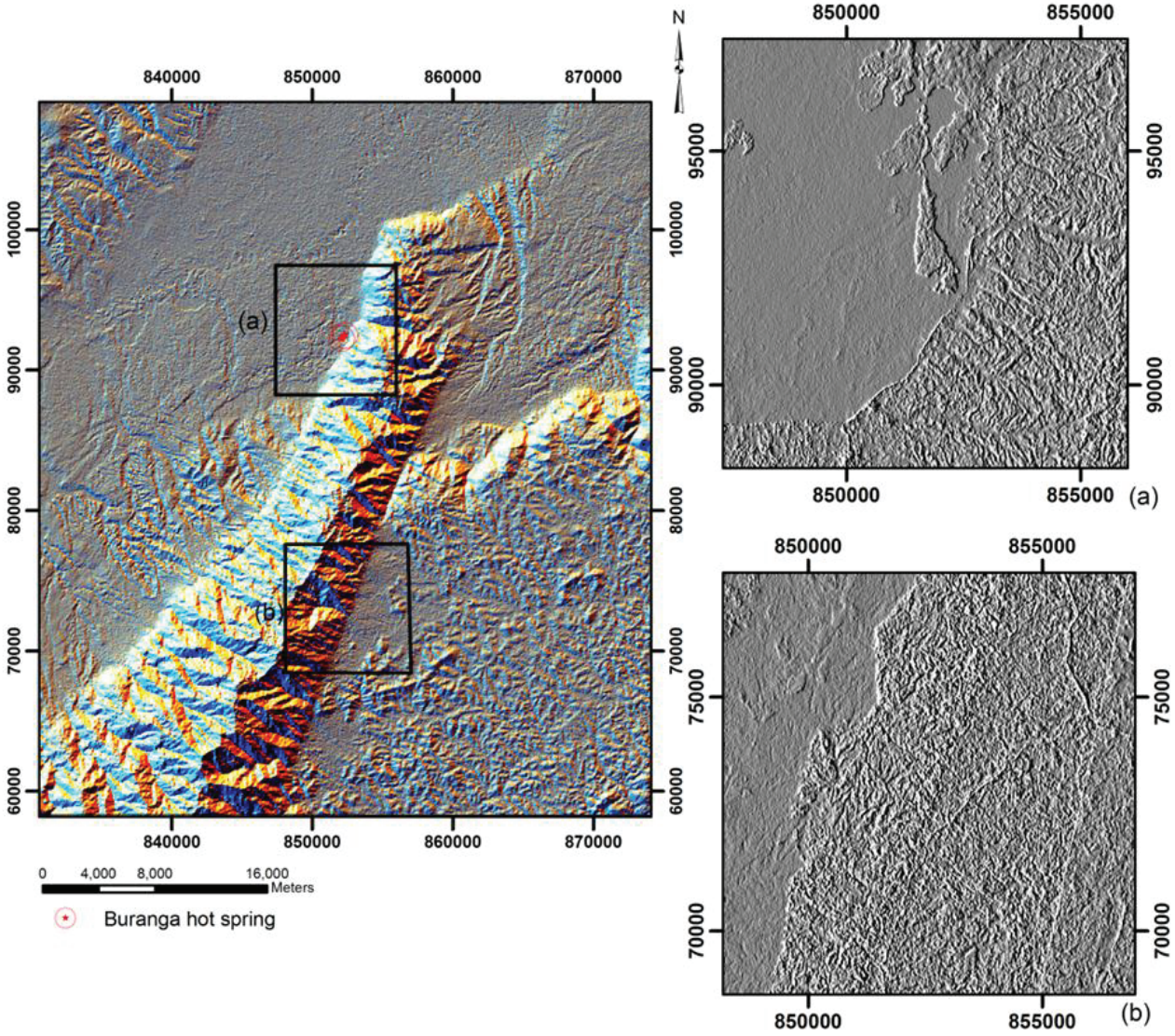

Figure 4.11: 3D hill shaded DEM of ASTER Global DEM version 2 (left); zoomed images of Directional filtered ASTER band 2

Because of the high resolution, ASTER three directional hill shaded DEM shows even the vegetation height differences as linear features. Although the band combination 7:4:2 was created to identify the structures, it doesn't seem to have much detail on the geological structures. However, this band combination is useful to separate the lineaments which seem due to the vegetation height difference, forest margins and lineament. This combination shows vegetation in green, water in blue. Hence the linear features which caused by vegetation height difference, forest margin could be neglected while analysis (Figure 4.2).

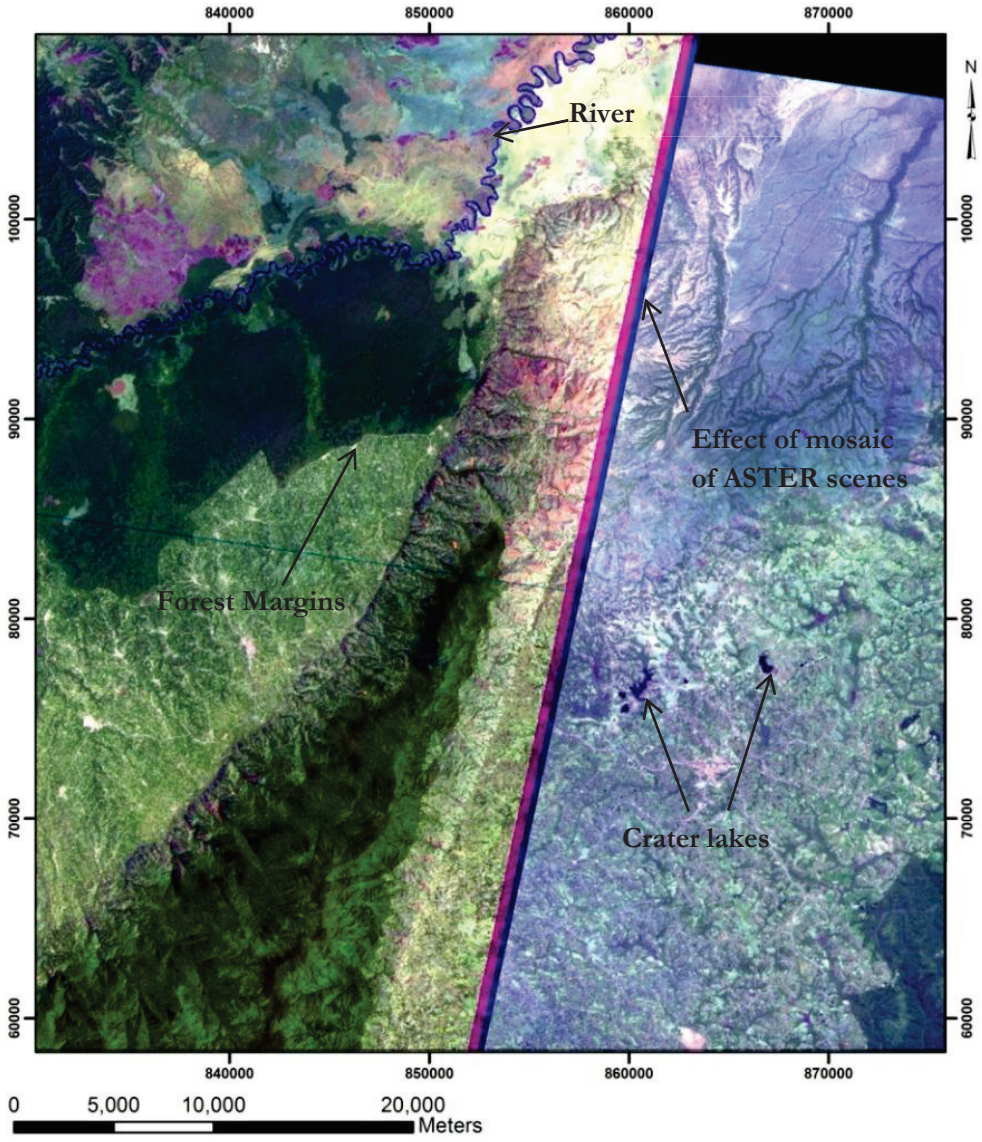

Figure 4.12: ASTER band combination 7:4:2

The manually interpreted surface structures exhibit some linear patterns and few crated lakes east to the Ruwenzori Mountain (Figure 4.13). Based on the direction of the lineaments shown in the rose diagram (figure 4.14), two major lineament systems can be identified. Those are the most frequent NW trending system and the NE to ENE trending system. These two systems are comparable with the field identification of fault systems on the Ruwenzori mountain top by Koehn, et al (2008). Therefore it can be suggested that that those systems are related with the Achaean basement rocks. And also NW system could be steeply dipping and the NE to ENE system is moderately dipping.

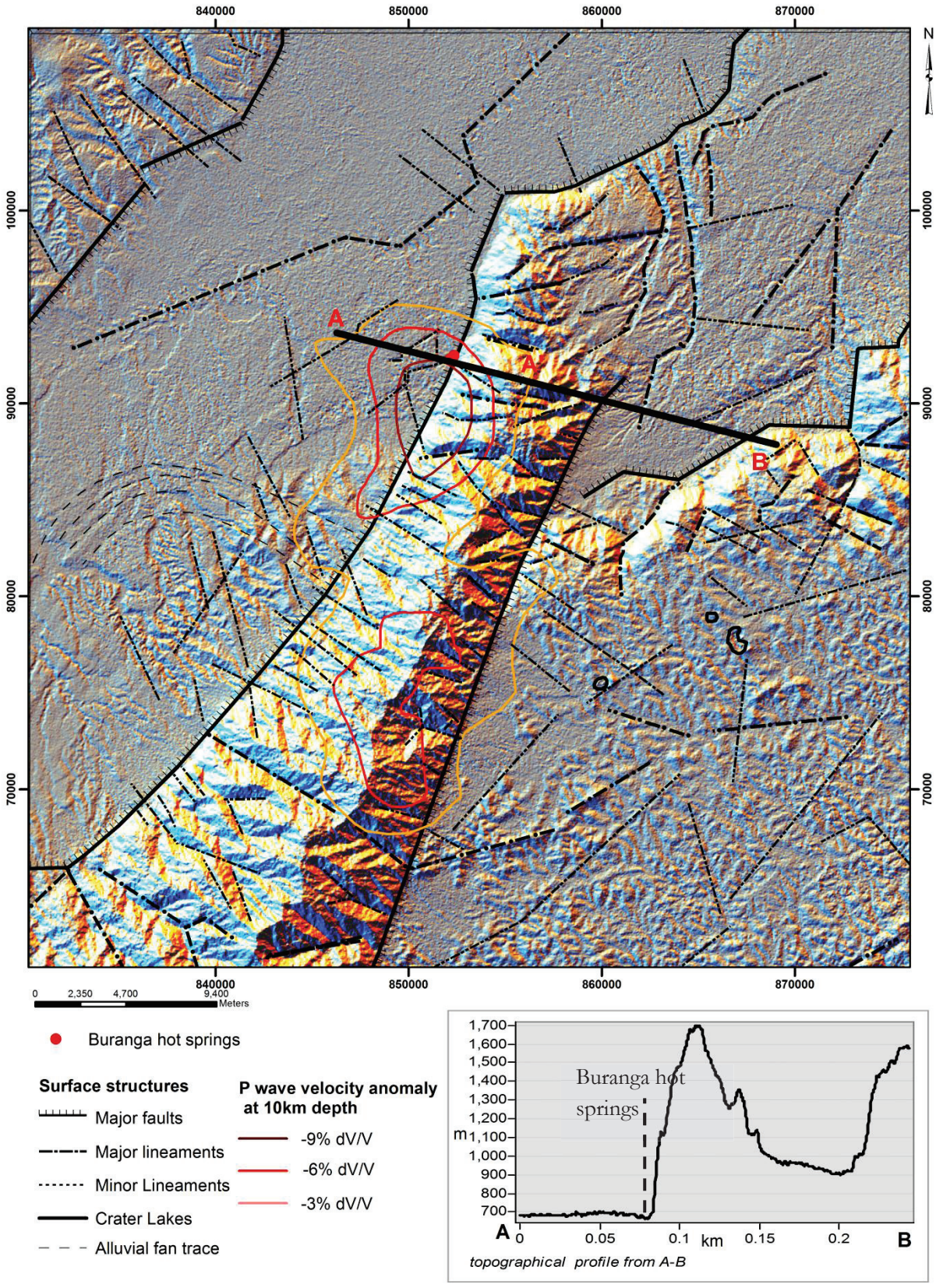

Figure 4.13: Structural interpretation with 10km depth seismic P wave velocity anomaly

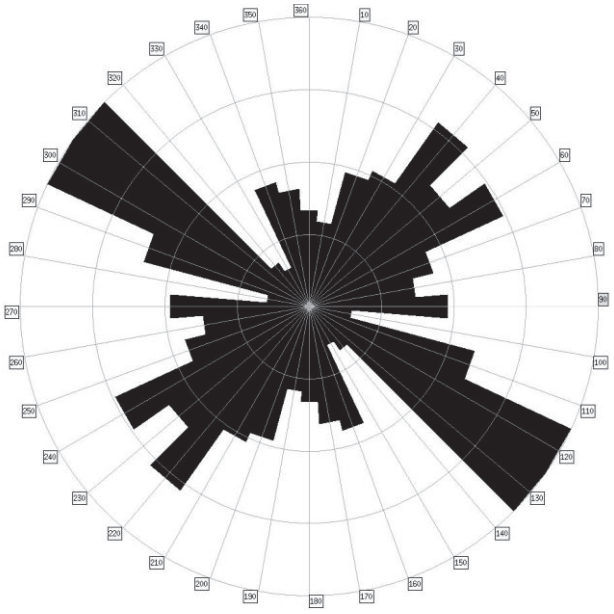

Figure 4.14: Rose diagram showing direction and frequency of lineaments

shows horst and graben structures which are characteristic for continental rift valley systems. The Ruwenzori Mountain block forms a horst structure and the valleys form the grabens.

Most of the lineaments identified on the rift valley are along the streams and river. The identification of the structure on the rift valley is hindered by sediment cover and the dense vegetation (D. Koehn, et al., 2008). Therefore those minor structures identified from the image may not represent real structures and may be visible due to vegetation height difference and drainage. There is no much supportive data to determine whether those linear features penetrate through the subsurface.

However, these linear features follow the directions of the rift valley faults and the structures on the basement rocks. Hence, these lineaments may portray subsurface linear features like rift valley faults or the fractures on the basement rock.

The major visually identified structures are the NNE trending faults which demarcate the Albertine rift valley zone and the outcropping Ruwenzori mountain. This system is not prominent in the rose diagram as the number of the faults is less copaere to the frequency of the other two systems.

As shown in the 2D topographic profile perpendicular to the major rift valley along A-B (Fig 4.12), both sides of the Ruwenzori mountain are steep due to faulting. The major rift valley faults have a normal fault movement (D. Koehn, et al., 2008). In the normal fault movement the hanging wall is moving downward with reference to the foot wall. The formation of the steep slopes has been resulted with this movement. These extensional faults have been formed during the rift development (Ebinger, 1989). Structurally, this area

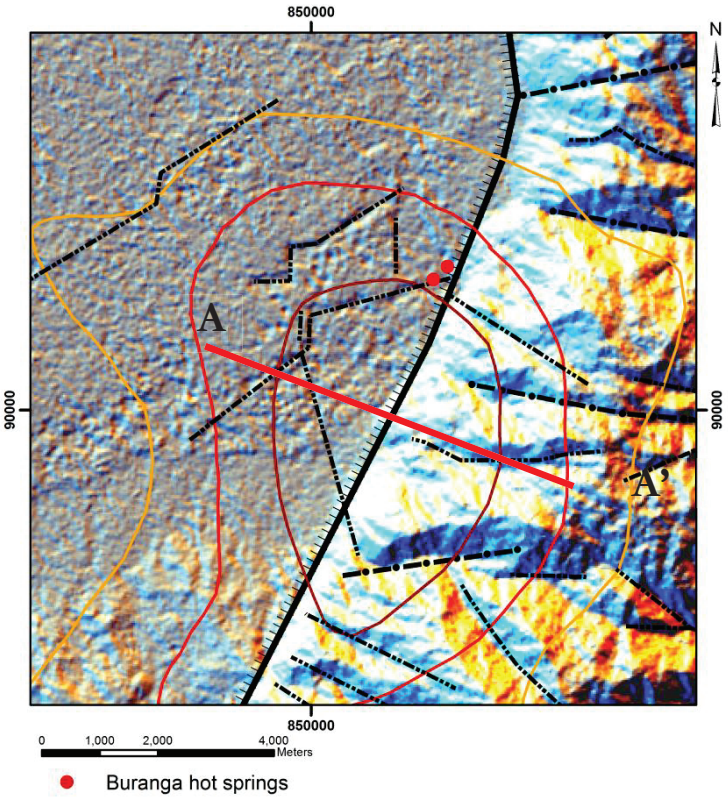

Figure 4.15: Structures around Buranga hot spring (Refer to the legend of Figure 4.12)

As shown from the structural interpretation closer to the hot spring locations (Figure 4.15), Buranga hot springs are close to the major rift valley fault and also to the NE minor lineament. The hot spring

locations plotted almost on the lineament trending NE direction. The trending and location of this lineament is similar with the hot spring fault which has been mentioned by Bahati (1998).

The crater lakes which are visible on the eastern side of the Ruwenzori Mountain (Figure 4.12) reflect the possible volcanic activities around the area and the rift related volcanic rocks evidence for it (Figure 2.3). So far no one has mentioned about any geothermal activity around that area.

4.5. Data integration

To understand the link between surface geothermal expressions and the surface geological structures, the Buranga hot spring locations and associated faults were projected towards the subsurface heat source by drawing vertical cross section (Figure 4.17) along the line A to A perpendicular to the Buwapa fault. The line is shown in the Figure 4.16 (a). The P wave velocity anomaly contour values till the depth of 10km were identified using the geo-referenced horizontal tomographic slices which are shown in the Figure 4.16.

The normal fault bounding the western flank of Ruwenzori mountain dips to the north west. As mentioned by Koehn et al. (2008), this fault is dipping with an angle of 65^0. However there is no any indication of the geometry of the minor lineaments closer to the Buranga hot springs. It was assumed that minor lineaments (fractures) are vertical. The ground level of the rift valley (Elevation= 800m) was considered as the base level for the reason that the seismometers had been mounted on the rift valley as mentioned by Ochmann et al. (2010).

The extended Buwampa fault coincide with the values (<-4% dV/V) of the seismic P wave velocity anomaly at 6-7 km depth (Figure 4.17). In the drawn cross section, the tomographic P wave velocity anomaly contours shows bending towards left(towards rift valley) at about 5-6 kms. The movement direction is shown red arrows in Figure 4.17. Looking at the different depth profiles (Figure 4.16), it is visible as the higher anomalies near the surface (1-5km) clusters towards the rift valley more than below the Ruwenzori Mountain. This movement may occur along a weak zone running NW direction in the the subsurface.

And also the contour lines of the P wave velocity anomaly on the vertical cross section seems moving along the Buwampa fault from about 5km to upward. This can be suggested as the hot magma from the heat source is upwelling through the Buwampa fault (since it is a weak zone) to some extend and has given this anomalous shape. This anomaly along the Buwampa fault may indicate the heated up basement rocks with upwelling hot magma. The hot spring fault splays off the major fault connecting the hot degassing magma body to the hot spring. This observations corresponding with the conceptual model suggested by Ochmann et al. (2010) (Figure 2.8). The figure 4.17 indicates the detailed subsurface situation around Burnga hot spring than the conceptual model of Ochmann et al. (2010). As mentioned by Bahati (1998), the geochemistry of the Buranga spring water indicate the presence of the magmatic heat body. Meteoric water percolating top through faults on Ruwenzori mountain may mixes with the magmatic flow or magmatic gaseous flow may cause for the chemical composition of the hot spring water.

Therefore, it can be suggested that the geothermal system in Buranga hot spring area is structurally controlled and the areas where the P wave anomalies are clustering towards rift fault system seems to be geothermally potential in study area.

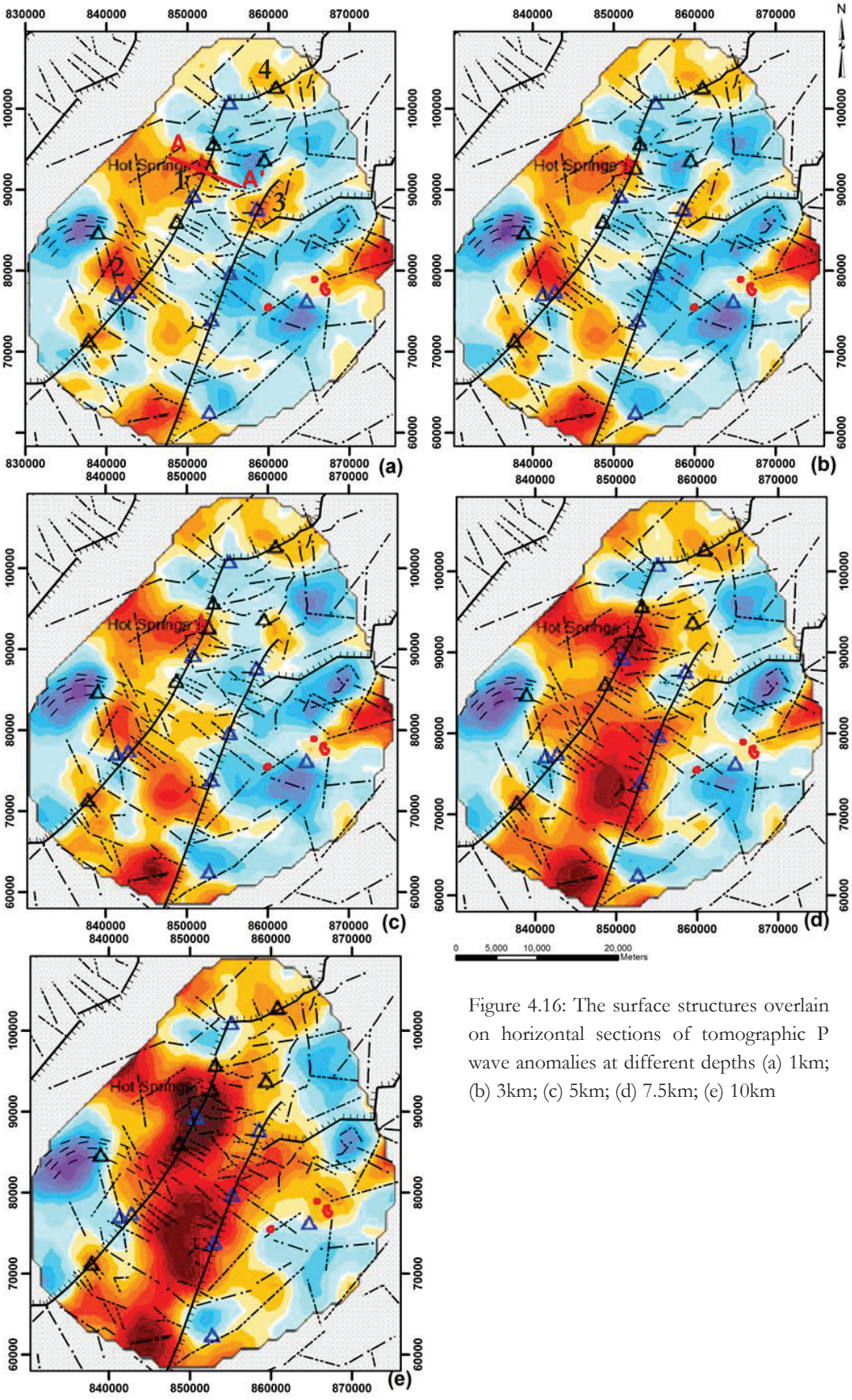

Figure 4.16: The surface structures overlain on horizontal sections of tomographic P wave anomalies at different depths (a) 1km; (b) 3km; (c) 5km; (d) 7.5km; (e) 10km

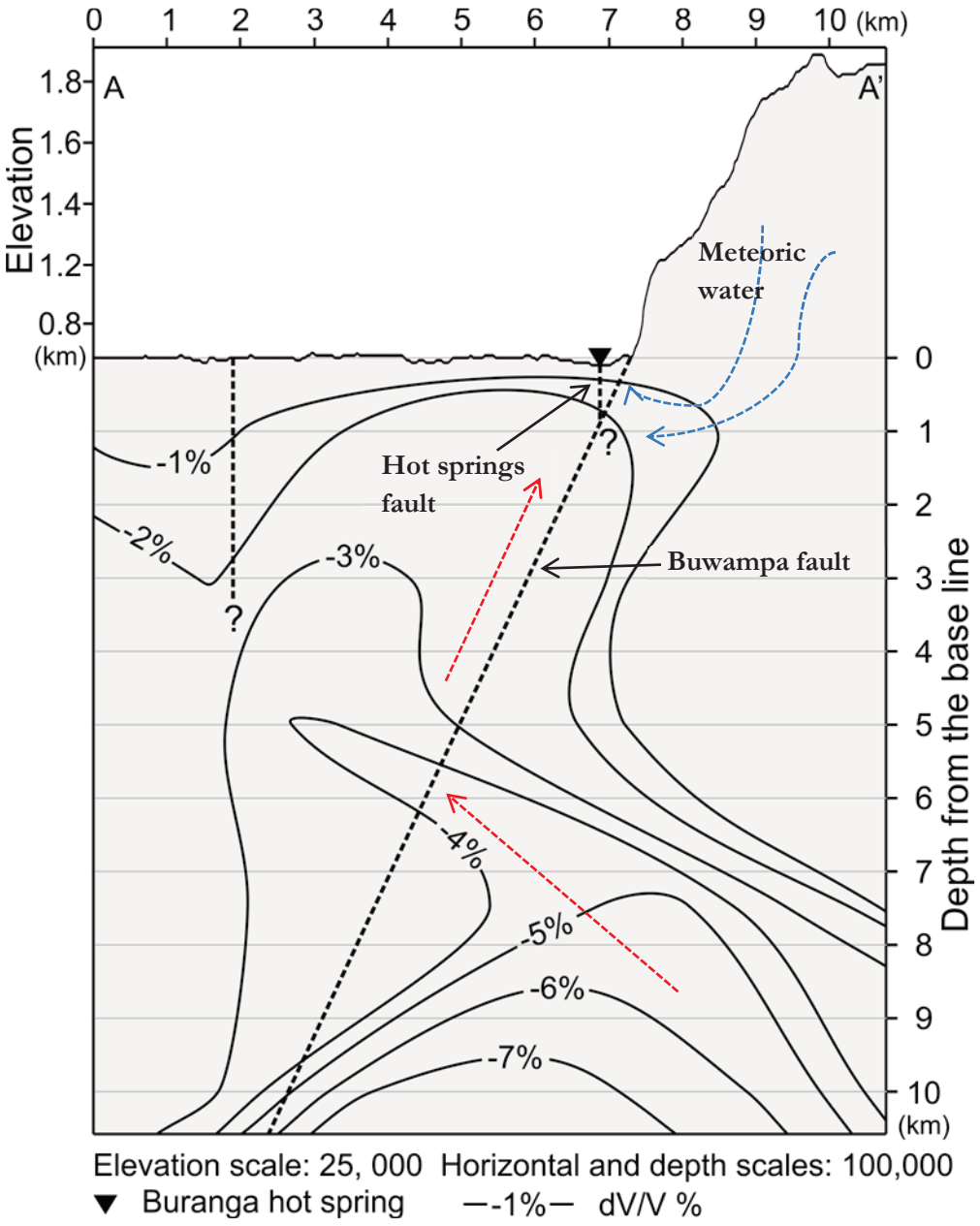

Figure 4.17: Integrated P wave velocity anomalies and geological structures shown as a vertical cross section along A-A' in figure 4.16

There are three more interesting areas (except the area with Buranga hot spring) based on the localization of P wave anomaly near the surface around 1 to 5 km (Figure 4. 16 (a). Those areas has numbered as 2,3 and 4 in the figure (Figure 4. 16 (a). However there is no any record on the hot springs positioning closer or on those areas.

Area 2 shows high P wave velocity anomalies closer to the Buwampa fault and the area is rich with minor lineaments (fractures). However area seems to be covered with thick alluvium fan sediment. The less permeability of the surface may restrict the movement of the hot water to the surface.

The eastern side of the Ruwenzori Mountain also shows a Normal fault (Ruimi-wasa fault). As shown by Koehn et al, (2008)., the fault dips towards west with an angle of 85^0 . The area 3 and 4which is located at the north eastern and north side of the Ruwenzori may also have the same condition for the absence of the hot springs. Few more cross sections has to be created cross cutting those areas to understand more on the link with subsurface seismic wave anomalies.

To find out the association of the Al-OH, Mg-OH and gypsum mineral content maps with the subsurface heat source and geological structures, P wave velocity anomaly at 1km depth and geological structures were overly on each mineral maps (Figure 4.18).

The Al-OH containing minerals rich areas are mostly in the river and stream systems (Figure 4.3 (a)). This indicates deposition of the clay minerals on the flood plains which comes from the washing of the higher mountainous areas. Also at the western foot of the Ruwenzori Mountain, occurrence of the Al-OH containing minerals was observed. This is running along the major rift valley fault. This may be due to the altering of the basement rocks in the presence hot fluid rising through the Buwampa fault. Or else, this may be due to the deposition of the weathered rock materials originated from the Ruwenzori Mountain top. The band ratio for the Al-OH containing minerals gives the indication of content of the minerals such as phengite, muscovite, paragonite,, lepidolite, illite,, brammalite,, montmorillonite,, beidellite,, kaolinite, dickite (Cudahy, 2011). The Ruwenzori Mountain is composed of granitic gneiss and contains feldspar as a dominant mineral. The weathering or altering of feldspar minerals also leads to the formation of clay minerals (Berner et al., 1979).

Comparing with the known mineral occurrences, the circular feature at the east to the Ruwenzori mountain indicate the occurrence of clay. This is where the volcanic rocks and crater lakes located. This circular feature may indicate a volcanic caldera. The altered volcanic rocks are responsible for the Al-OH content. This area may indicate a fossil hydrothermal field as a volcanic caldera.

The Mg-OH minerals are present mostly over the open sediments areas. The image band ratio for Mg-OH containing minerals, indicates the calcite, dolomite, magnesite, chlorite, epidote, amphibole, talc, serpentine (Cudahy, 2011). The highest Mg-OH containing minerals distribution is in the rift valley area north of the Ruwenzori mountain (figure 4.3 (c). This is connected to the southern end of the Albert lake where in this case the values may be related to the carbonate minerals in the calcareous sandstone. The patchy occurrence of the Mg-OH along the road at the eastern side if the Ruwenzori mountain indicates the build up areas on cleared land. This may be the whole rift valley system is giving the Mg-OH coning mineral signature due to the carbonate minerals in sediments. But it has been masked by the vegetation and visible only where the land was cleared for agriculture or constructions.

With the exiting data on mineral occurrences it shows that gypsum is coinciding with the known mineral occurrence gypsum at the north nose of Ruwenzori mountain (NO4 in Figure 4.18(d)). This can be related to the geothermal actives over the area as there is a seismic p wave anomaly is visble at the 1km depth. And also oil seepage is also prominent there. The formation of gypsum in this area may be associated with oil seepages. The sulphur content in the hydrocarbon leads to the formation of gypsum (Shi et al., 2010). The area NO4 in Figure 4.18(d) may be interesting on geothermal actives and has to be further studies. Gypsum is occurs at the area no5 (Figure 4.18 (d)) within is a low elevated area within the rift valley. This may indicate the formation of gypsum as evaporates in rift valley.

However, the used band ratios for the identification of mineral alterations mapped mostly the mineral content in Sediment cover over the area.

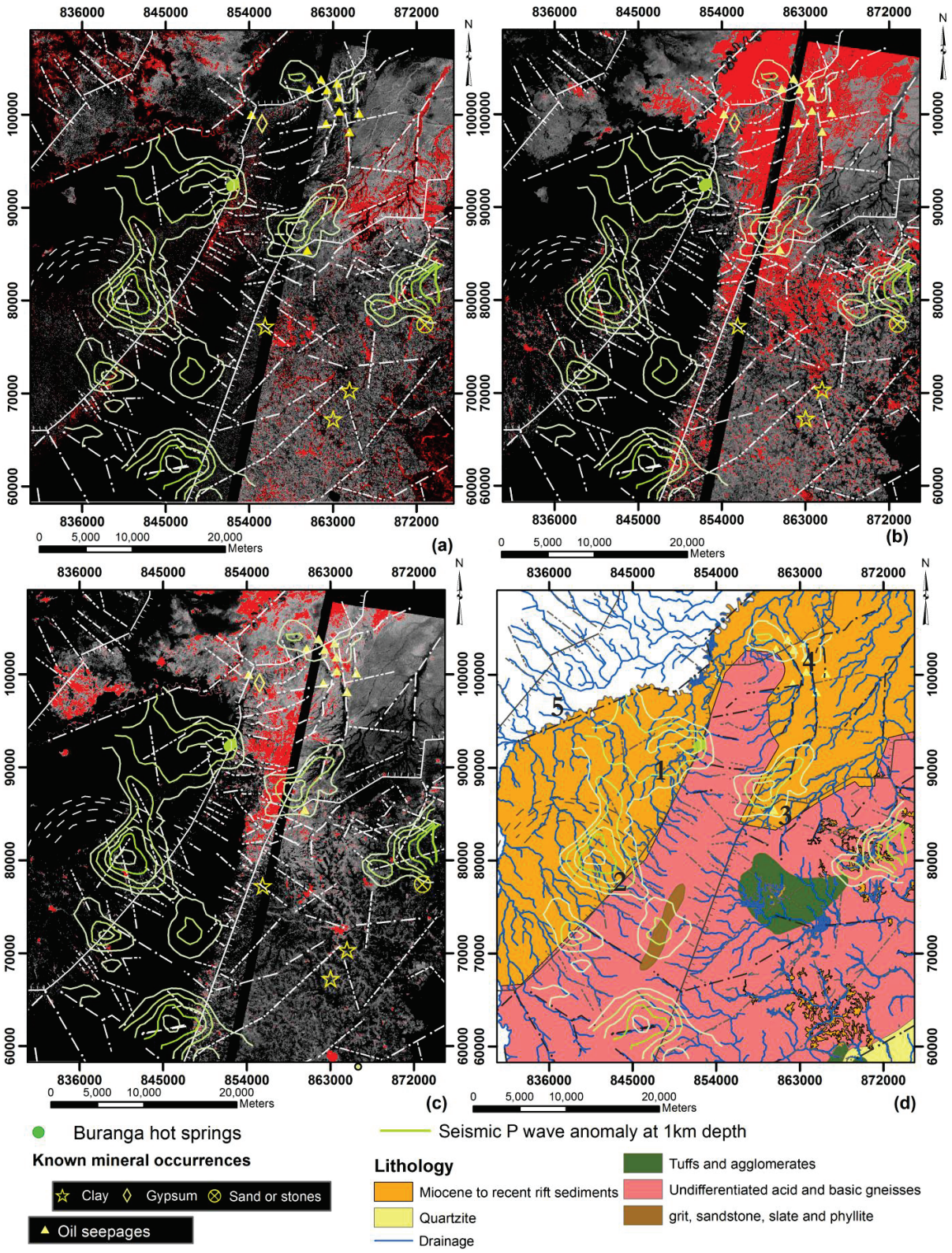

Figure 4.18: Mineral maps of the study area(a) Al-OH containing mineral map; (b) Mg-OH containing mineral map; (c) gypsum mineral occurrence map; (d).Lithology (1:250,000 geological map from Geological Survey of Uganda) and drainage network system (P wave velocity anomalies at 1km depth and, Buranga hot spring and surface geological structures has overly on top of each image)

5. CONCLUSIONS AND RECOMMEDATIONS

5.1. Conclusions

The following conclusions were made based on the results gain through the analysis of available data.

Occurrences of Al-OH, Mg-OH and gypsum mineral content were mapped using the ASTER multispectral band ratio method. However these results seem to be associated with the mineral composition of rift valley sediments. The occurrence of Al-OH containing minerals closer to the Buranga hot spring may indicates the alterations due to the geothermal fluids. Circular feature on the Al-OH mineral content map (on the area of volcanic rock exposures) indicates clay minerals after the hydrothermal alterations of volcanic rocks.

Temperature variation over the study area is mostly related to the elevation difference, vegetation and the high heat capacity of the water bodies in the area. Thermal anomalies detected using MODIS night thermal images are sensible for the diurnal changes of the temperature of the materials an annual change in the land cover. The thermal anomalies visible in the area using the hot spot identification method pinpoint few pixels as hotspots and those points did not give any connection to the known geothermal locations. The moisture content and vegetation around hot spring hinders the identification of thermal anomalies due to geothermal heating.

Three main systems of lineaments were identified as geological structure. NNE normal faults demarcating the rift valley and Ruwenzori mountain block; and two linear features trending NW and NE to ENE on basement rock and also on the rift valley. The Buranga hot spring is located on one of the NE trending lineament on the rift valley.

The hot spring locations are closely associated to the Buwampa normal fault and also close to the minor lineaments. The integration of seismic P wave velocity anomalies and surface structures at Buranga hot spring displays that the P wave anomalies moves along the Buwampa fault. This concluded that the heat related to the Buranga hot spring may have gain through the upwelling magma along the Buwampa fault. Therefore the Buranga hot springs and the heat source seem to be associated together with the rift valley normal faults of the area.

5.2. Recommendation

It's recommended to use high spatial resolution images like ASTER infrared night time imagery to identify of thermal anomalies. The day time thermal mages with high resolution can also use to identify the hot spots with necessary corrections for the topographic effect, emissivity and so on.

For the structural interpretation the geophysical data like magnetic is required to identify more subsurface structural features in order to link between the subsurface and surface features.

Field work must be carried out to identify the geology, mineral occurrences and geological structures of the area in detail for further verification and spectral characteristics of the lithology should be collected.

The annual changes present on thermal anomalies can be further study using a time series analysis.

LIST OF REFERENCES

Abrams, M., Hook, S., & Ramachandran, B. (2002). ASTER user handbook (Vol. 2, pp. 1-135).

Bahati, G. (1998). Soil temperature survey of the Buranga geothermal field, West Uganga.

Bahati, G. (2004). Status of geothermal exploration in Uganda. Paper presented at the Presented at Short Course II on Surface Exploration for Geothermal Resources,
organized by UNU-GTP and KenGen, at Lake Naivasha, Kenya.

Bahati, G., Pang, Z., Ármannsson, H., Isabirye, E. M., & Kato, V. (2005). Hydrology and reservoir characteristics of three geothermal systems in western Uganda. Geothermics, 34(5), 568-591.

Berner, R. A., & R., H. G. (1979). Mechanism of feldspar weathering—II. Observations of feldspars from soils. Geochimica et Cosmochimica Acta, 43(8), 1173-1186.

Calvin, W., Coolbaugh, M., & Vaughan, R. G. (2002). Geothermal site characterization using multi and hyperspectra imagery. Geothermal Resource Cuncil Transactions, 26, 483-484.

Chorowicz, J. (2005). The East African rift system. Journal of African Earth Sciences, 43(1-3), 379-410.

Coll, C., Caselles, V., Valor, E., Niclòs, R., Sánchez, J. M., Galve, J. M., et al. (2007). Temperature and emissivity separation from ASTER data for low spectral contrast surfaces. Remote Sensing of Environment, 110(2), 162-175.

Coolbaugh, M. F., Kratt, C., Fallacaro, A., Calvin, W. M., & Taranik, J. V. (2007). Detection of geothermal anomalies using Advanced Spaceborne Thermal Emission and Reflection Radiometer (ASTER) thermal infrared images at Bradys Hot Springs, Nevada, USA. Remote Sensing of Environment, 106(3), 350-359.

Coolbaugh, M. F., Lechler, P., Sladek, C., & C., K. (2009). Carbonate tufa columnsas exploration guides for geothermal systems in thegerat basin. GRC Transactions, 33.

Cudahy, T. (2011). Satellite ASTER Geoscience Product Notes, Western Australia.

Dozier, J. (1981). A method for satellite identification of surface temperature fields of subpixel resolution. Remote Sensing of Environment, 11(0), 221-229.

Drury, S. A. (2001). Image interpretation in geology (Third edition ed.). Cheltenham, Malden: Nelson Thornes, Blackwell Science.

Ebinger, C. J. (1989). Tectonic development of the western branch of the East African rift system. Geological Society of America Bulletin, 101(7), 885-903.

Eggermont, H., Russell, J., Schettler, G., Van Damme, K., Bessems, I., & Verschuren, D. (2007). Physical and chemical limnology of alpine lakes and pools in the Rwenzori Mountains (Uganda–DR Congo). Hydrobiologia, 592(1), 151-173.

Eneva, M., Coolbaugh, M., & Combs, J. (2006). Application of satellite Thermal Infrared imagery to geothermal exploration in east central California. GRC Transactions, 30.

Gozzard, J. R. (2006). Image processing of aster multispectral data. Geological survey of western Australia.

Hanano, M. (2004). Contribution of fractures to formation and production of geothermal resources. In: Renewable and sustainable energy reviews, 8(2004)3, pp. 223-236.

Hecker, C. A., Kuenzer, C., & Zhang, J. (2007). Remote sensing based coal - fire detection with low resolution MODIS data. In: Geology of coal fires : case studies from around the world / ed by G.B. Stracher. Boulder : Geological Society of America (GSA), 2007. (Geological Society of America Reviews in Engineering Geology ; XVIII) ISBN 978-0-8137-4118-5 pp. 229-238.

Hewson, R. D., Cudahya, T. J., Mizuhikob, S., Uedac, K., & Mauger, A. J. (2005). Seamless geological map generation using ASTER in theBroken Hill-Curnamona province of Australia. Remote Sensing of Environment, 99, 159-172.

Horler, D. N. H., Dockray, M., Barber, J., & Barringer, A. R. (1983). Red edge measurements for remotely sensing plant chlorophyll content. Advances in Space Research, 3(2), 273-277.

ILWIS. (2007). ILWIS 3.31 Academic help, ITC.

Jones, K. L., & Schulenburg, N. W. (2010). Hyperspectral remote sensing techniques for locating geothermal areas. Paper presented at the Active and Passive Signatures.

Koehn, D., Aanyu, K., Haines, S., & Sachau, T. (2008). Rift nucleation, rift propagation and the creation of basement micro-plates within active rifts. Tectonophysics, 458(1–4), 105-116.

Koehn, D., Lindenfeld, M., Rümpker, G., Aanyu, K., Haines, S., Passchier, C., et al. (2010). Active transsection faults in rift transfer zones: evidence for complex stress fields and implications for crustal fragmentation processes in the western branch of the East African Rift. International Journal of Earth Sciences, 99(7), 1633-1642.

Kratt, C., Calvin, W., & Coolbaugh, M. (2006). Geothermal exploration with Hymap hyperspectral data at Brady–Desert Peak, Nevada. Remote Sensing of Environment, 104(3), 313-324.

Kühn, M. (2004). 2 Concepts, Classification, and Chemistry of Geothermal Systems Reactive Flow Modeling of Hydrothermal Systems (Vol. 103, pp. 11-46): Springer Berlin / Heidelberg.

Lillesand, T. M., Kiefer, R. W., & Chipman, J. W. (2004). Remote sensing and image interpretation (Fifth edition ed.). New York etc.: Wiley & Sons.

Maasha, N. (1975). The Seismicity of the Ruwenzori Region in Uganda. Journal of geophysical research, 80(11), 1485-1496.

NASA. (2004). Latest features image from aster.

Natukunda, J. F. (2010). Geology of Kibiro, Katwe and Buranga Geothermal Prospects of Uganda. Proceedings World Geothermal Congress 2010 Bali, Indonesia.

Nemec, W. (1988). The shape of the rose. Sedimentary Geology, 59(1–2), 149-152.

Ochmann, N., Kraml, M., Babirye, P., & Lindenfeld, M. (2010). Microearthquake Survey at the Buranga Geothermal Prospect, Western Uganda. Proceedings World Geothermal Congress 2010, Bali, Indonesia.

Ochmann, N., Kraml, M., Lindenfeld, M., Yakovlev, A., Rumpker, G., & Babirye, P. (2008). Microeathquake Survey at the Buranga Geothermal Prospect (Western Uganda) within the scope of GEOTHERM, the German Program for promoting the Utilization of Geothermal Energy in developing contries. Paper presented at the Riftlink Workshop, Germany.

Paplinski, A. P. (1998). Directional filtering in edge detection. Image Processing, IEEE Transactions on, 7(4), 611-615.

Pastor, M. S. (2010). Application of Thermal Remote Sensing for Geothermal Mapping, Lake Naivasha, Kenya. Proceedings World Geothermal Congress 2010 Bali, Indonesia.

Pirasteh, S., Pradhan, B.,Safari, H.,Ramli, M. (2011). Coupling of DEM and remote-sensing-based approaches for semi-automated detection of regional geostructural features in Zagros mountain, Iran. Arabian Journal of Geosciences, 1-9.

Rockwell, B. W., & Hofstra, A. H. (2008). Identification of quartz and carbonate minerals across northern Nevada using ASTER thermal infrared emissivity data-Implications for geologic mapping and mineral resource investigations in well-studied and frontier areas Geosphere, 4(6), 992-992.

Roller, S., Hornung, J., Hinderer, M., & Ssemmanda, I. (2010). Middle Miocene to Pleistocene sedimentary record of rift evolution in the southern Albert Rift (Uganda). International Journal of Earth Sciences, 99(7), 1643-1661.

Rumpker, G., Lindenfeld, M., & Yakovlev, A. (2007). Detailed surface analysis, earthquake localization andtravel-time tomographyS: University of frankfurt.

Saemundsson, K. (2010). East African rift system -an overview. Presented at Short Course V on Exploration for Geothermal Resources,organized by UNU-GTP, GDC and KenGen, at Lake Bogoria and Lake Naivasha, Kenya.

Savtchenko, A., Ouzounov, D., Ahmad, S., Acker, J., Leptoukh, G., Koziana, J., et al. (2004). Terra and Aqua MODIS products available from NASA GES DAAC. Advances in Space Research, 34(4), 710-714.

Shi, P., Fu, B., & Ninomiyab, Y. (2010). Mapping Hydrocarbon Seepage Induced Anomalies in the Arid Region, West China Using Multispectral Remote sensing. International Archives of the Photogrammetry, Remote Sensing and Spatial Information Science, XXXVIII, 442-446.

USGS. (2011). METI and NASA Release Version 2 ASTER Global DEM. from https://lpdaac.usgs.gov/about/news_archive/monday_october_17_2011

Van Damme, D., & Pickford, M. (1998). The late Cenozoic Viviparidae (Mollusca, Gastropoda) of the Albertine Rift Valley (Uganda—Congo). Hydrobiologia, 390(1), 171-217.

Wang, Q., & Tenhunen, J. D. (2004). Vegetation mapping with multitemporal NDVI in North Eastern China Transect (NECT). International Journal of Applied Earth Observation and Geoinformation, 6(1), 17-31.

Woldegabriel, G., L., A. J., & Walter, R. C. (1990). Geology, geochronology, and rift basin development in the central sector of the Main Ethiopia Rift. Geological Society of America Bulletin, 102(4), 439-458.

www.climatetemp.info. Uganda Climate Guide to the Average Weather and Temperatures. Access on 12th of November 2011

www.lpdaac.usgs.gov. aster_products_table. Access on 30th of October 2011

Zhang, J., Wagner, W., & van Dijk, P. M. (2004). Spatial and statistical analysis of thermal satellite imagery for extraction of coal fire related anomalies. Vienna University of Technology, Vienna.

APPENDICES

Appendix 1

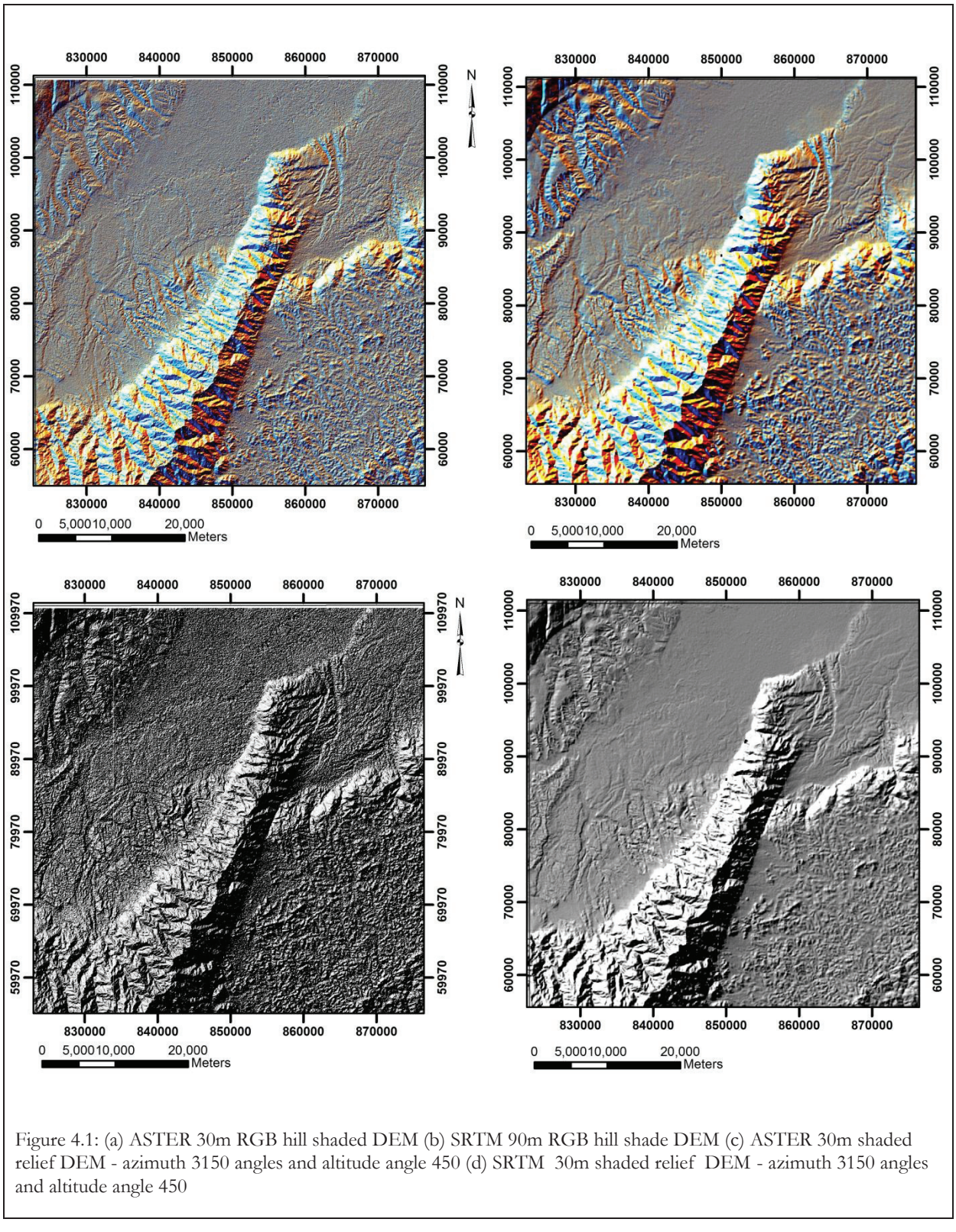

Figure 4.1: (a) ASTER 30m RGB hill shaded DEM (b) SRTM 90m RGB hill shade DEM (c) ASTER 30m shaded relief DEM - azimuth 3150 angles and altitude angle 450 (d) SRTM 30m shaded relief DEM - azimuth 3150 angles and altitude angle 450